Remodeling adipocytes' lipid metabolism with a polycation loaded enzyme-active framework reverses osteoporotic bone marrow

Wenzheng Lin[1,2,3,4], Suyu Gu[1,3,4], Xing Zhang[1], Ke Li[1,2,3], Duoyi Zhao[1,2,3], Biao Ma[1,2,3], Chun Pan[1,3], Zhuobin Xu[1,3], Tingting Liu[2], Huihui Wang ![ORCID][1,3] ✉, Sihan Hu[1,3] ✉ & Hao Chen ![ORCID][1,2,3] ✉

The function of osteoporosis-induced bone marrow adipocyte (BMAds) accumulation remains inadequately understood. Here, we analyze bone marrow lipidomic data and reveal that BMAds deteriorate the skeletal microenvironment by secreting large amounts of lipids, altering the senescence status of neighboring cells by affecting their mitochondrial function. To specifically target BMAds under osteoporotic conditions, we design a polycation-loaded biomimetic dual-site framework (CZP@LC) that interferes with lipid crosstalk between BMAds and neighboring bone marrow cells. Shutting down abnormal lipid metabolism and secretion in adipocytes mitigates mitochondrial dysfunction in neighboring cells, which prevents bone marrow cells from senescing. The inhibition of lipid synthesis in BMAds blocks bone marrow stromal cells from differentiating into adipocytes, interrupting the vicious cycle. Moreover, interruption of lipid communication rescues osteoblasts from mitochondrial dysfunction-induced senescence and restores osteogenesis. Here we demonstrate the metabolic mechanisms of BMAds and lipid crosstalk in osteoporosis, provide a potential avenue for targeted biotherapy.

Accumulation of adipocytes within the bone marrow cavity results in the formation of bone marrow adipose tissue (BMAT), which plays a crucial role in numerous physio-pathological processes[1,2]. The prevailing consensus in the field of osteoporosis is that the proliferation of bone marrow adipocytes (BMAds) may influence the function of other cell populations through the secretion of a range of biologically active molecules, including lipids, cytokines, chemokines and adipokines[3–6]. Studies have even shown that senescent BMAds may induce secondary senescence of neighboring cells through the senescence-associated secretory phenotype (SASP), which ultimately results in the accumulation of aging cells and an abnormal bone marrow microenvironment[7]. However, how BMAds directly affect neighboring cells in the bone marrow via abnormal lipid accumulation is still unclear.

In addition to the role of BMAds in the secretion of SASP factors that influence cellular senescence, we speculate that the fatty acids released by these adipocytes can independently induce senescence in adjacent cells, including bone marrow stromal cells (BMSCs) and osteoblasts. This could be attributed to the fact that lipids that accumulate in the bone marrow act as bioactive molecules that interfere

[1]Institute of Translational Medicine, Medical College, Yangzhou University, Yangzhou, P. R. China. [2]Department of Orthopedics, Affiliated Hospital of Yangzhou University, Yangzhou, P. R. China. [3]The Key Laboratory of the Jiangsu Higher Education Institutions for Nucleic Acid & Cell Fate Regulation, Yangzhou, P. R. China. [4]These authors contributed equally: Wenzheng Lin, Suyu Gu. ✉e-mail: wanghh56@yzu.edu.cn; shhu28@yzu.edu.cn; hchen2020@yzu.edu.cn

with the physiological function of osteoblasts, leading to rupture or fragmentation of the mitochondrial membrane by excessively increasing mitochondrial fatty acid oxidation (FAO) and altering the mitochondrial membrane potential[8,9]. Moreover, studies have demonstrated that disruption of the homeostatic balance of mitochondria is an important cause of cellular senescence[10,11]. The senescence of BMSCs or osteoblasts further weakens their osteogenic ability, which disrupts the homeostasis of the bone marrow[12–15], leading to the collapse of the bone marrow in the osteoporotic microenvironment. Consequently, we propose that the accumulation of BMAds in osteoporosis may play a crucial role in the imbalance of the overall bone marrow microenvironment by releasing excess fatty acids, leading to dysfunction of fatty acid oxidation in the mitochondria of other cells, which contributes to the increase in the number of senescent cells in the bone marrow by affecting the homeostasis of mitochondrial function. Therefore, targeted interference with lipid metabolism in BMAds could be a potential approach to reduce the degree of cellular crosstalk that worsens in osteoporotic conditions.

Cationic nanomaterials, represented by polyamidoamine (PAMAM) dendritic polymers, have been demonstrated to have significant potential in the therapeutic management of inflammatory diseases and cancer through their neutralization of negatively charged pathogens[16,17]. In osteoporosis, the expansion of BMAT increases the concentration of the extracellular matrix, especially the most highly negatively charged glycosaminoglycans[18,19]. Therefore, polyamidoamine generation 3 (PG3), characterized by the presence of strong cations on its surface, could be enriched in BMAT to inhibit lipid synthesis[20,21]. However, this inhibition is not complete because residual lipids continue to promote adipogenic differentiation via lipid peroxidation (LPO), which is mediated by the key enzyme LPCAT3[22]. Hence, integrating the *Lpcat3*-CRISPR/Cas9 (LC) gene editing plasmid into PG3 could be a more effective approach, as PG3 is also a gene carrier for DNA transfection[23]. Additionally, the effect of PG3 was further attenuated by the high amount of ROS in the osteoporotic microenvironment. To improve the delivery efficiency and mitigate the amount of reactive oxygen species (ROS) in the microenvironment, a biomimetic copper (Cu) ion-doped traditional ZIF8 structure (Cu/Zn-ZIF8) was introduced as a carrier[24,25]. The bimetallic doping structure mimics the bimetallic center of natural Cu/Zn-superoxide dismutase (SOD), thus imparting antioxidant activity to consume ROS in the microenvironment as well.

Briefly, we use Cu/Zn-ZIF8 as an effective drug delivery vehicle and utilize its highly porous nature to encapsulate PG3@LC to form a CZ-PG3@LC (CZP@LC) nanoplatform. The PG3@LC released from the nanoplatform in the slightly acidic environment targeted the BMAds to interfere with lipid metabolism while attenuating the promotional effect on adipogenesis caused by LPO (Fig. 1). The composite nanoplatform reshapes lipid metabolism to achieve rescue of osteoblast mitochondrial dysfunction by interfering with the intercellular lipid crosstalk mechanism to effectively promote osteogenic differentiation, providing an innovative strategy for the treatment of osteoporosis from a cellular lipid metabolic perspective.

Results

BMAds accumulation and lipid metabolism significantly increase in osteoporotic bone marrow

The tendency of BMSCs to differentiate toward BMAds rather than osteoblasts is one of the key drivers in the pathogenesis of osteoporosis[26]. Its contribution to the bone marrow microenvironment is not clear. Therefore, alterations in BMAds and osteoblasts were observed by simulated osteoporosis at different time points after ovariectomy (OVX). Microcomputed tomography (μCT) analysis revealed a significant reduction in bone mass in OVX mice (Fig. 2A–C and Supplementary Fig. 1A, B), which is consistent with previous studies[27]. Hematoxylin and eosin (HE) and immunofluorescence

staining revealed that the number of "vacuolar ghost cells", which represent BMAds in the femoral sections, increased significantly with increasing time after OVX (Fig. 2D, E). Oil red O (ORO) staining revealed that as osteoporosis progressed, lipid droplets were distributed around the BMAds and occupied the entire marrow cavity (Supplementary Fig. 2A, B). Moreover, costaining of p21 with osteocalcin (OCN) revealed a significant overlap in the OVX mice, indicating a marked increase in osteoblast senescence (Supplementary Fig. 2C–E). As BMAds are the major source for lipid synthesis and secretion, to comprehensively understand the lipid landscape within these cells, femoral lipidomic analysis of the BMAds in mice 8 weeks after OVX or sham surgery was carried out (Fig. 2F). On the basis of the LIPID MAPS database, our enrichment analysis of differential lipids revealed that acylcarnitine and fatty acid (FA) are the lipids that exhibit significant changes in osteoporotic bone marrow (Fig. 2G). The accumulation of acylcarnitines results from excessive mitochondrial FAO rates[28,29], confirming that significantly increased lipids in the bone marrow lumen may contribute to mitochondrial dysfunction, which triggers cellular senescence. These results suggest that the accumulation of BMAds and their lipid metabolism within osteoporotic bone marrow could be potentially detrimental factors that destroy the entire bone marrow microenvironment.

Polyunsaturated fatty acids (PUFAs) in bone marrow facilitate BMSC adipogenesis and exacerbate osteoblast mitochondrial dysfunction

Since FAs are major energy sources for cells and act as molecules involved in signal transduction, we further analyzed the different lipids contributing to the fatty acid pathway. According to the results of the lipidomic analysis, the three fatty acids associated with the FA pathway were FA (18:1), FA (20:4) and FA (18:0). FA (20:4), commonly referred to as arachidonic acid (AA), was significantly greater in the bone marrow of OVX mice than in that of the sham group (Fig. 2H). Moreover, the enzyme-linked immunosorbent assay (ELISA) results demonstrated a positive correlation between the levels of AA and increasing weekly age in the OVX group (Supplementary Fig. 3). On this basis, AA was selected for subsequent investigations aiming to reveal the impact of lipids on the cells neighboring the BMAds within the osteoporotic bone marrow. To verify the effect of AA on the differentiation of BMSCs, the cells were induced with or without AA to induce adipogenesis (ADI) or osteogenesis (OSI), and ORO and alkaline phosphatase (ALP) staining revealed that the presence of AA increased adipogenesis but impaired osteogenesis in the BMSCs (Fig. 2I, J). Furthermore, the similarly elevated FA (16:0) identified via lipidomic analysis, palmitic acid, consistently exhibited inhibitory effects on osteogenesis while promoting adipogenesis in BMSCs (Supplementary Fig. 4A, B). These data demonstrate that lipids, such as AA or palmitic acid, contribute to the exacerbation of adipogenesis in osteoporosis.

Moreover, to further validate the role of acylcarnitines and PUFAs in MC3T3-E1 mitochondrial dysfunction, we added a fatty acid agonist (GW1929) or a fatty acid antagonist (GW9662) to MC3T3-E1 cells after coculture with BMSCs (induced or uninduced adipogenesis), respectively. Subsequently, JC-1 and MitoSOX staining confirmed that GW9662 rescued the mitochondrial dysfunction in MC3T3-E1 cells caused by BMAds obtained from BMSCs after the induction of adipogenesis (Fig. 2K). Next, MC3T3-E1 cells were exposed to AA to further model the role of excessive lipid metabolism in osteoblasts after OVX, particularly with respect to mitochondrial function and osteoblast senescence. By transmission electron microscopy (TEM), we found that the number of mitochondrial cristae in AA-treated osteoblasts was significantly reduced and that mitochondrial fragmentation even occurred (Supplementary Fig. 5A). Moreover, the JC-1 probe revealed that AA decreased the mitochondrial membrane potential (Supplementary Fig. 5B). Furthermore, mitochondrial superoxide was significantly increased by AA (Supplementary Fig. 5C), which led to an
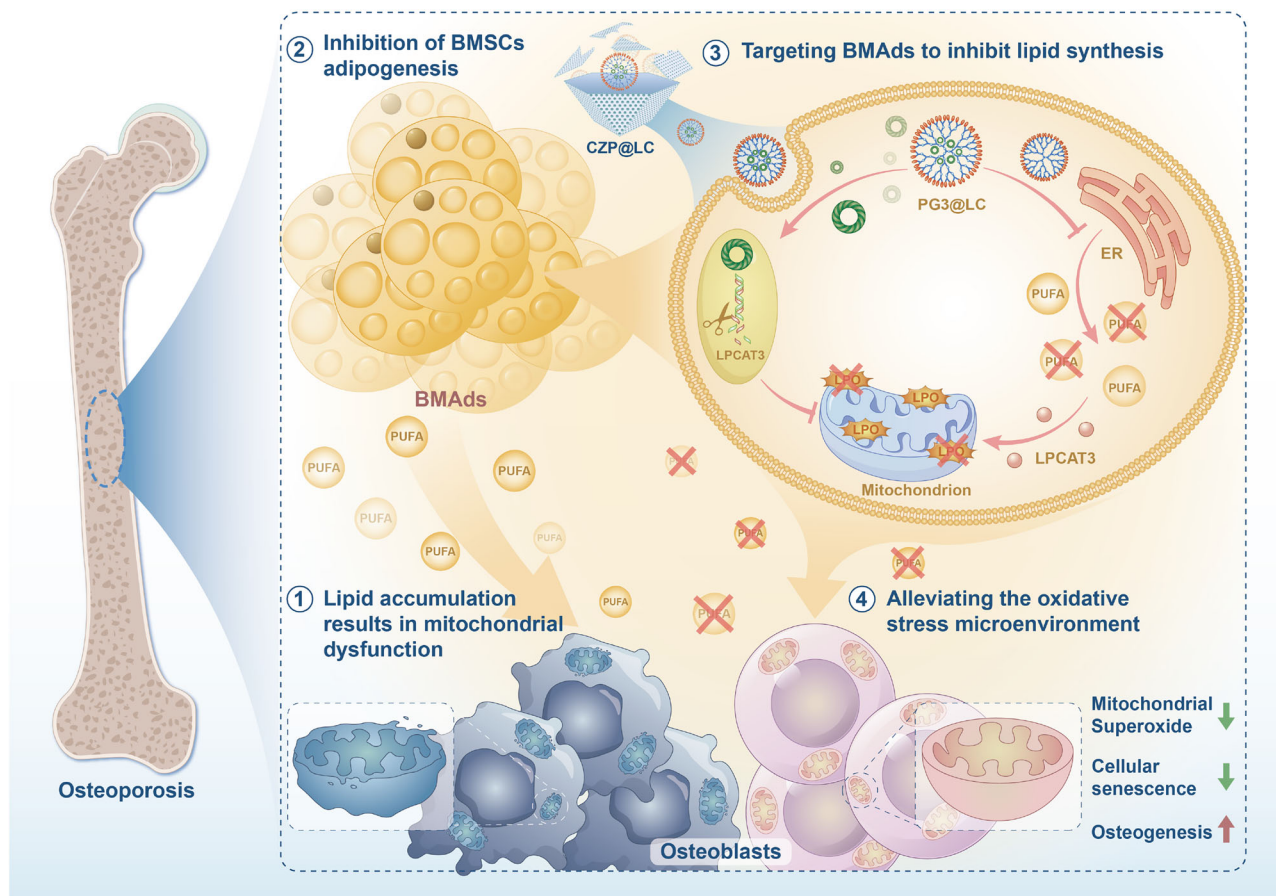
Fig. 1 | Schematic diagram of CZP@LC regulation of BMAds lipid metabolism. CZP@LC rescues collapsed bone marrow in osteoporotic conditions through targeted remodeling of lipid metabolism in bone marrow adipocytes.

imbalance in mitochondrial homeostasis. Next, to determine whether AA aggravates osteoblast senescence via FAO, MC3T3-E1 cells were incubated with AA. Senescence-associated beta-galactosidase (SA-β-gal) staining revealed that osteoblasts presented obvious senescence (Supplementary Fig. 5D). To further elucidate the potential mechanism of AA-induced mitochondrial dysfunction in MC3T3-E1 cells, GW9662 or GW1929 was added in the presence or absence of AA, respectively. Immunofluorescence confirmed that GW9662 suppressed the expression of PINK1 and PARK2, suggesting that mitochondrial dysfunction was effectively restored (Fig. 2L). These results suggest that excess lipids such as AA impair cellular mitochondrial functional homeostasis, thereby leading to cellular senescence and impaired osteogenic capacity.

Construction and characterization of CZP@LC

To alleviate the adverse consequences of the abundant lipids secreted by the BMAds, CRISPR/Cas9 plasmids that can inhibit *Lpcat3*, a key enzyme in this process, were constructed and loaded onto PG3 (Supplementary Fig. 6A). Different ratios of PG3 and plasmids were mixed at 4 °C for 1 day to test the efficiency of PG3 piggyback, and agarose gel electrophoresis revealed that the LC plasmid was completely loaded when the ratio was 1:1 (Supplementary Fig. 6B). On this basis, CZP@LC was synthesized via the one-pot method to warp the LC-loaded PG3, and the details of the construction process are shown in Fig. 3A. TEM images of Cu/Zn-ZIF8 (CZ), Cu/Zn-ZIF8-PG3 (CZP), Cu/Zn-ZIF8@LC (CZ@LC), and Cu/Zn-ZIF8-PG3@LC (CZP@LC) revealed distinct and well-defined morphologies (Fig. 3B). Elemental mapping and energy dispersive X-ray spectroscopy (EDS) further confirmed that the elements zinc (Zn) and Cu were uniformly

distributed in the nanoframework (Fig. 3C and Supplementary Fig. 6C). The above data clearly show that the morphology of the synthesized nanoplatform was not affected by the addition of either the PG3 or the LC plasmid, indicating its original stability and consistency. A previous study demonstrated that the osteoporotic bone marrow microenvironment is acidic[30,31]. Therefore, various nanoplatforms containing LC plasmids were placed in acidic solvents, and the loading stability of the plasmids was assessed via agarose gel electrophoresis. As shown in Fig. 3D, all the nanoplatforms exhibited robust stability under neutral conditions. However, most of the CZ@LC plasmids were released when the pH was 6.0, while the plasmids piggybacked by PG3 were still securely loaded. These results indicate that PG3@LC is highly effective at preventing leakage within the acidic microenvironment of the bone marrow.

The average hydrodynamic particle sizes of CZ, CZP, CZ@LC and CZP@LC in water were 86.48 ± 11.86, 80.30 ± 14.34, 86.13 ± 19.72, and 78.57 ± 6.89 nm, respectively. Moreover, all the nanoplatforms presented low particle dispersion indices (PDI), indicating that they were well dispersed (Fig. 4A). High surface potentials are critical for targeting BMAds. Hence, the significantly higher zeta potential of CZP indicates that PG3 was successfully loaded. Furthermore, the zeta potential of CZP@LC was slightly lower than that of CZP, possibly because the negative charge of the LC plasmid partially neutralized the positive charge of PG3 (Fig. 4B). However, CZP@LC still maintains a high positive charge, which is sufficient for the targeting of BMAds. The powder X-ray diffraction (XRD) pattern suggested that the characteristic peaks of the synthesized nanoplatforms were consistent (Fig. 4C). X-ray photoelectron spectroscopy (XPS) demonstrated consistent elemental and chemical valence states
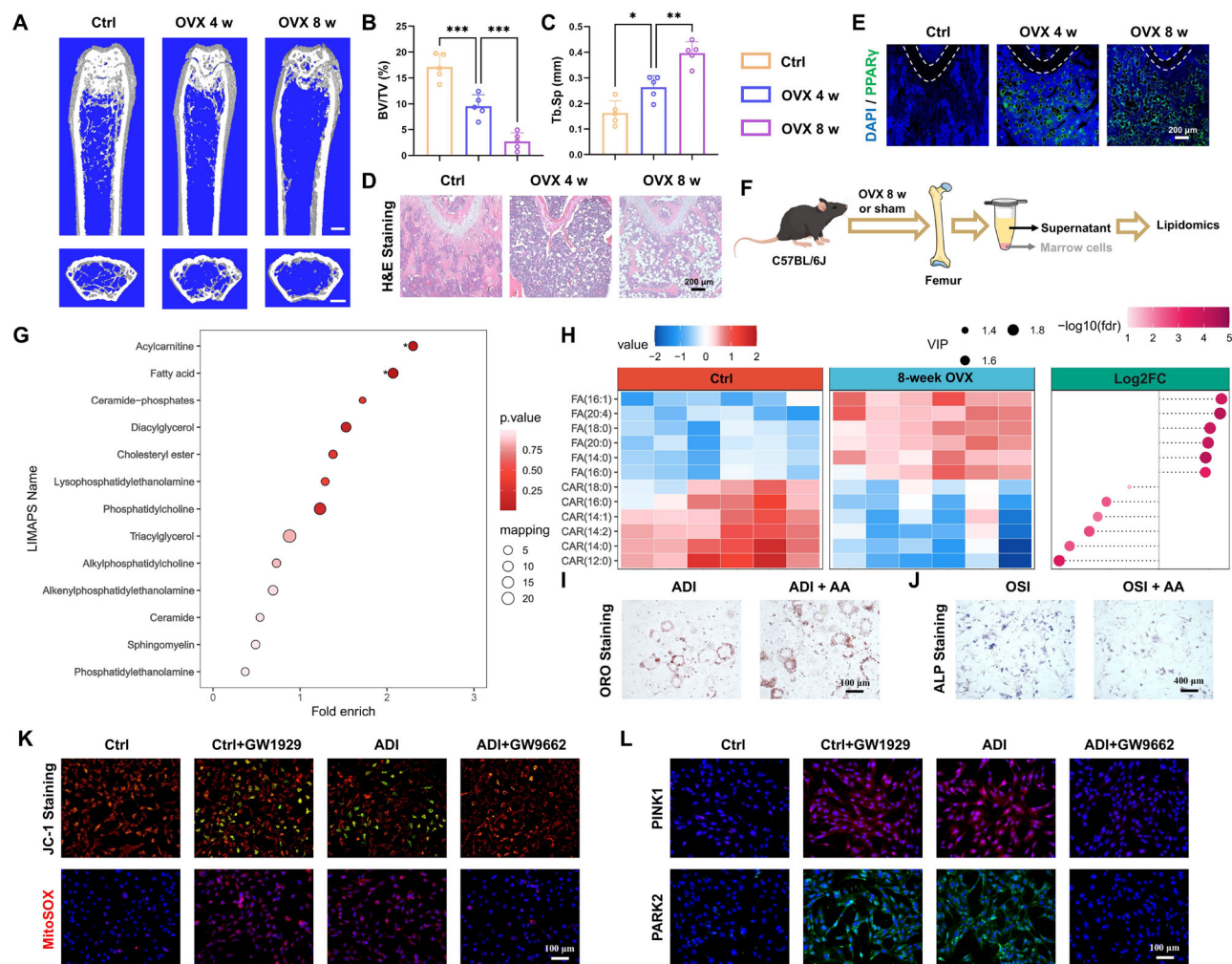
Fig. 2 | The accumulation of bone marrow adipocytes (BMAds) alters the microenvironment. A Representative microcomputed tomography (μCT) images of mouse femurs from the control group or after 4 or 8 weeks of ovariectomy (OVX) (scale bars: 0.5 mm). **B**, **C** Quantitative μCT analysis of bone volume per tissue volume (BV/TV) and trabecular separation (Tb.Sp) was performed on femurs ($n = 5$). **D**, **E** Representative images of HE staining and immunofluorescence images of PPARγ after 4 or 8 weeks of OVX and the control. **F** Simplified schematic representation of the lipidomic analysis. **G** Bubble plots of LIPID MAPS functional categorical enrichment analysis (8-week OVX vs control, $n = 6$ mice). **H** Differential lipid thermograms of the control and 8-week OVX groups ($n = 6$ mice). **I**, **J** Representative images of Oil Red O (ORO) staining or alkaline phosphatase

(ALP) staining after bone marrow mesenchymal stem cell (BMSC) differentiation via adipogenic induction (ADI) or osteogenic induction (OSI) with or without the addition of AA. **K** MC3T3-E1 cells were treated with fatty acid agonists (GW1929) or antagonists (GW9662) after coincubation with bone marrow stromal cells (BMSCs) (with or without ADI) for JC-1 or MitoSOX staining. **L** Representative images of immunofluorescence staining for PINK1 or PARK2 after various treatments. The data were expressed as the means ± SDs. Statistical significance was determined by one-way ANOVA. *$p < 0.05$, **$p < 0.01$, ***$p < 0.001$. (Mouse element from Figdraw (www.figdraw.com) are used in this figure. Microtube and femur elements adapted from Servier Medical Art (https://smart.servier.com/) are used in this figure, licensed under CC BY 4.0 (https://creativecommons.org/licenses/by/4.0/)).

across all the constructed groups (Fig. 4D–G). Fourier transform infrared spectroscopy (FT-IR) revealed that the surface functional groups and chemical bonds of the nanoplatforms were consistent, with no other bands present in the infrared spectra, which further suggested that the loaded drug was encapsulated in the crystal structure (Fig. 4H). These results provide additional evidence that the addition of PG3 or LC plasmids does not alter the crystal structure properties of metal–organic frameworks. Next, to evaluate chemical stability and biodegradability, CZP@LC was dissolved in an acidic solvent (pH 6.0) free of metal, and inductively coupled plasma (ICP) was used to determine the concentration of elemental Zn at different times. Almost complete degradation of CZP@LC was detected on day 14, before which the degradation rate remained relatively stable, thus ensuring the sustained release of the loaded cargos (Fig. 4I). In addition, this result provides a reference for the subsequent dosing interval.

Enzyme-like activity of CZP@LC

High levels of ROS are major contributors to the development of osteoporosis[32]. Thus, elimination of ROS should serve as the initial step toward reducing the osteoporotic microenvironment. The synthesized CZP@LC nanoplatforms were found to possess enzyme-like activities, including those of SOD and CAT. The SOD enzyme demonstrates potent antioxidant properties by catalyzing the conversion of $\cdot O_2^-$ to H_2O_2 and O_2. As shown in Fig. 4J, the scavenging capacity of $\cdot O_2^-$ increased in a concentration-dependent manner with the addition of CZP@LC, which suggests that CZP@LC possesses significant SOD-like activity. Moreover, when CZP@LC was subjected to an acidic solution at pH 6.0, its SOD enzyme activity decreased in a time-dependent manner, which was attributed to the disruption of the Cu/Zn bimetallic center. Catalase (CAT) enzymes are recognized for their capacity to catalyze the decomposition of toxic H_2O_2 into O_2 and H_2O. Dissolved oxygen assays revealed that CZP@LC has notable CAT-like activity,
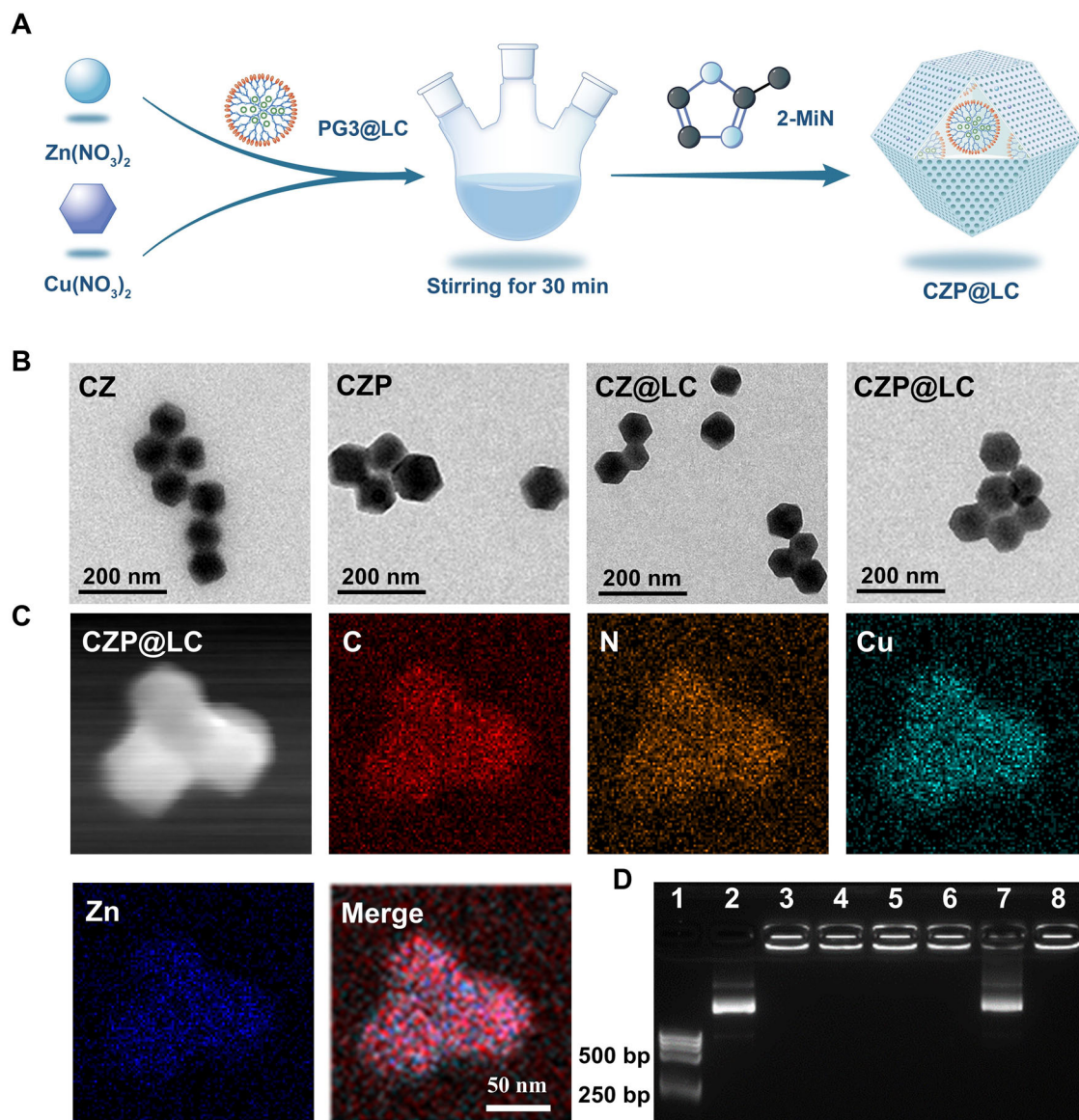
Fig. 3 | Construction and morphology of CZP@LC nanoplatforms. A Schematic of the synthesis of CZP@LC. **B** Representative transmission electron microscopy (TEM) images of CZ, CZP, CZ@LC, and CZP@LC. **C** Elemental mapping confirmed the presence of C, N, Cu, and Zn in CZP@LC. **D** Agarose gel electrophoresis of various nanoparticles; Lane 1: DNA hyperladder; Lane 2: pure LC plasmid; Lanes 3–5: PG3@LC, CZ@LC and CZP@LC treated at pH 7.4 for 2 days; Lanes 6–8: PG3@LC, CZ@LC and CZP@LC treated at pH 6.0 for 2 days.

efficiently metabolizing H_2O_2 and producing O_2 (Fig. 4K). In addition, •OH is a highly reactive free radical, and its removal is essential for maintaining the physiological functions of organisms and attenuating the aging process[33]. The results showed that CZP@LC has a comparable ability to scavenge •OH in a concentration-dependent manner with respect to its SOD and CAT enzymatic activities (Fig. 4L). Hence, CZP@LC, which has multiple enzymatic activities, is expected to serve as a potent pharmaceutical agent for combating ROS in the osteoporotic microenvironment.

The cytotoxicity of these nanoplatforms should be tested prior to confrontation experiments. The safe concentration of CZ and CZP@LC was 100 μg ml^{-1}, whereas the safe concentration of PG3@LC was 800 μg ml^{-1}, which still resulted in high cell survival (Supplementary Fig. 7A–C). The mitochondrial membrane potential was subsequently evaluated via JC-1 staining of MC3T3-E1 cells cocultivated with AA for 24 h and supplemented with CZ, CZP, CZ@LC, or CZP@LC solutions. A high level of J-monomers represents a low mitochondrial membrane potential. The mitochondrial membrane

potential was significantly rescued in these groups, with the level in the CZ@LC or CZP@LC groups increasing most obviously (Fig. 5A, B). Similarly, all these nanoplatforms, especially CZ@LC and CZP@LC, effectively reduced mitochondrial superoxide levels (Fig. 5C, D). The validation of the anti-ROS efficacy through dihydroethidium (DHE) staining demonstrated that, compared with other nanoplatforms, CZP@LC, which is loaded with the LC plasmid and PG3, significantly reduced ROS levels (Fig. 5E, F). Increased ROS are thought to cause cellular senescence[34], a process characterized by a notable increase in SA-β-gal activity. Specific staining for SA-β-gal was subsequently performed and was found to decrease significantly (Fig. 5G, H). Moreover, representative SASP factors released by senescent cells, such as IL-1β or TNFα, were further evaluated, with different levels of reduction observed in all the groups (Fig. 5I–L). Furthermore, in vivo DHE staining revealed a lower fluorescence intensity in the CZ- or CZ@LC-treated OVX mice than in the OVX group, especially in the CZP and CZP@LC groups (Fig. 5M, N). These results demonstrated that the constructed CZP@LC effectively alleviated the mitochondrial
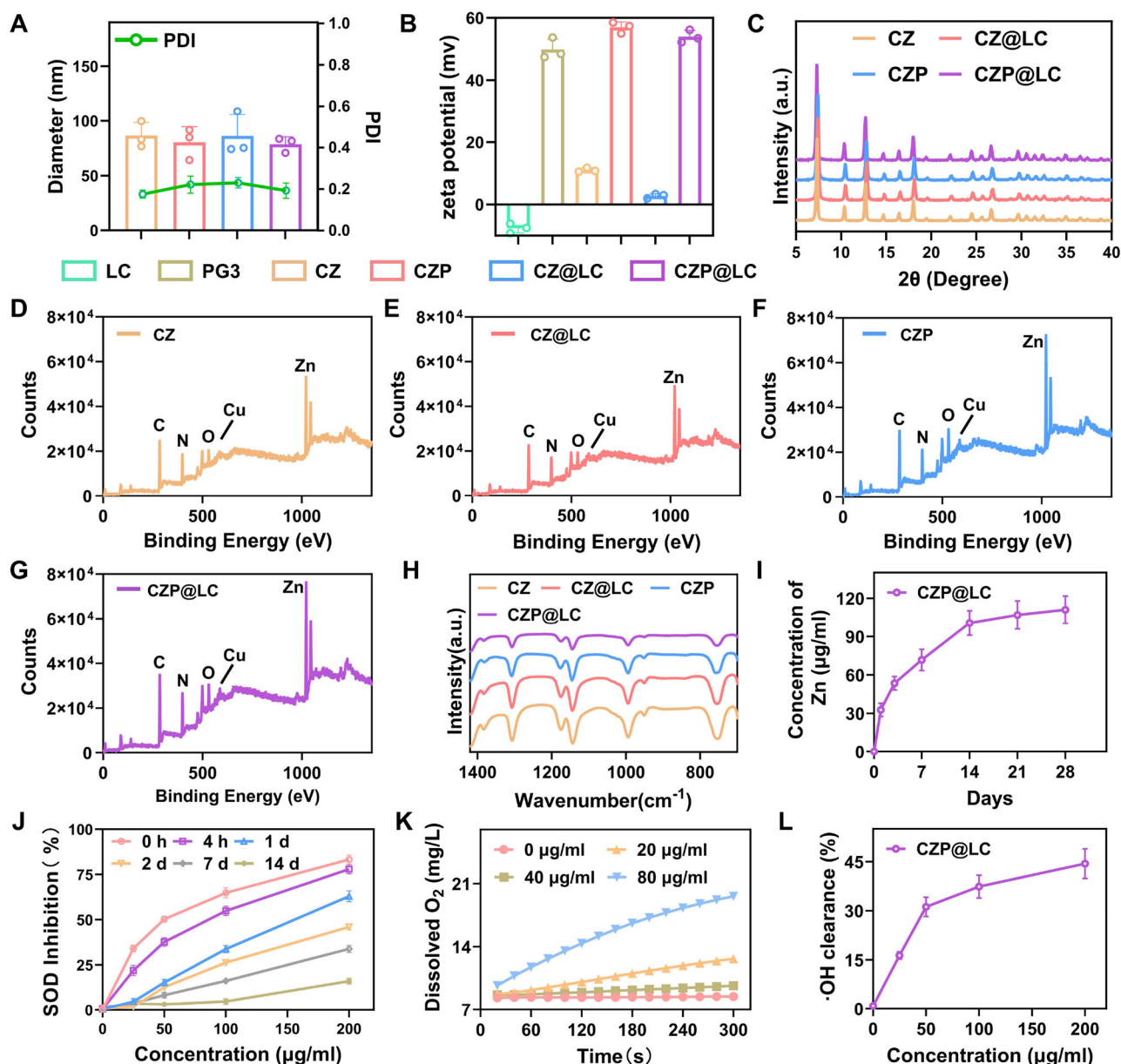
Fig. 4 | Enzyme-like activity and physicochemical characterization of CZP@LC.
A The average hydrodynamic particle size of various nanoplatforms ($n = 3$ independent experiments). **B** Zeta potential of the LC plasmid, PG3 and synthetic nanoparticles ($n = 3$ independent experiments). **C** powder X-ray diffraction (XRD) patterns of various nanoparticles. X-ray photoelectron spectroscopy (XPS) spectra of CZ (**D**), CZ@LC (**E**), CZP (**F**), and CZP@LC (**G**). **H** Fourier transform infrared spectroscopy (FT-IR) patterns of the synthetic nanoplatforms. **I** Inductively coupled plasma (ICP) was used to detect Zn in CZP@LC at different time points ($n = 3$ independent experiments). **J, K** The superoxide dismutase (SOD) -like and catalase (CAT) -like activities of CZP@LC were evaluated via a SOD activity assay kit and a dissolved oxygen meter ($n = 3$ independent experiments). **L** •OH scavenging capacity of CZP@LC ($n = 3$ independent experiments). The data were expressed as the means ± SDs.

dysfunction in osteoblasts caused by lipids in the osteoporotic microenvironment and mitigated cellular senescence.

CZP@LC presents ideal BMAds-targeting ability and LC plasmid transfection ability

To assess the ability of PG3 to target BMAds in vivo, mice at 8 weeks after OVX were injected with CZ@LC or CZP@LC into the bone marrow cavity. In the bone marrow, PPARγ is expressed predominantly in the BMAds population and plays a key role in adipocyte differentiation, maturation and functional maintenance. Therefore, evaluation of PPARγ⁺EGFP⁺ cell populations (EGFP, enhanced green fluorescent protein, originating from the LC plasmid) via flow cytometry after centrifugation of femoral bone marrow on days 0, 3, and 7 after

injection validated the ability of CZP@LC to target BMAds (Fig. 6A). The PPARγ⁺ cell population was approximately 54.9% on day 7, whereas the PPARγ⁺EGFP⁺ cell populations were 26.1 ± 2.01% and 45.3 ± 2.69% in the CZ@LC and CZP@LC groups, respectively, implying that the percentage of BMAds-targeting CZP@LC was approximately 82.5% (Fig. 6B–D). Moreover, caveolin-1 (CAV-1), which regulates adipocyte differentiation and plays a key role in adipocyte differentiation[35], also demonstrated consistent results (Supplementary Fig. 8A, B). Moreover, to further validate the ability of PG3 to target BMAds, Ce6-labeled CZP@LC (Ce6-CZP@LC) was injected into the femurs of the mice 8 weeks after OVX, and the BMAds and precipitated non-BMAds were separated via centrifugation. Fluorescence imaging confirmed that the binding of Ce6-CZP@LC to BMAds increased in a time-dependent
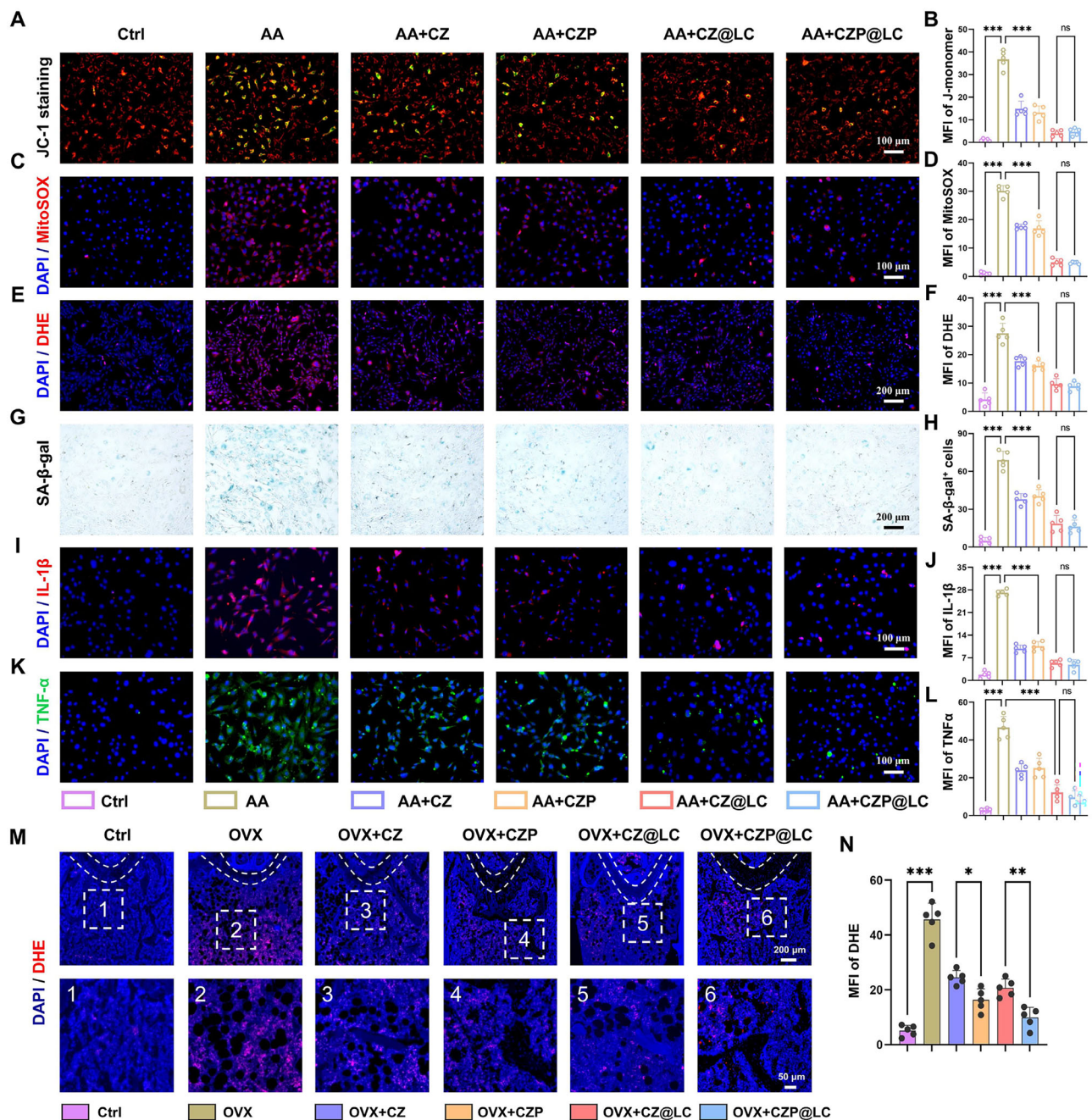
Fig. 5 | CZP@LC effectively alleviated mitochondrial dysfunction and rescued cellular senescence. A–D JC-1 and mitoSOX staining were used to detect and quantify the mitochondrial function of cells treated with AA and various nanoparticles ($n = 5$ independent experiments). **E–H** The nanoplatforms alleviated the oxidative stress and senescence caused by AA in MC3T3-E1 cells, as detected and quantified by dihydroethidium (DHE) staining and senescence-associated beta-galactosidase (SA-β-gal) staining ($n = 5$ independent experiments).

I–L Representative immunofluorescence images and quantitative analysis of IL-1β and TNF-α in the different groups ($n = 5$ independent experiments). **M, N** Representative images and quantitative analysis of DHE fluorescence staining of femoral sections ($n = 5$ mice). The data were expressed as the means ± SDs. Statistical significance was determined by one-way ANOVA. *$p < 0.05$, **$p < 0.01$, ***$p < 0.001$.

manner (Supplementary Fig. 8C, D). These results suggest that CZP@LC has greater transfection efficacy than CZ@LC does and that CZP@LC has superior targeting ability to BMAds.

Given that PG3 can target BMAds as well as LC plasmids harboring EGFP, cellular uptake could be verified by evaluating GFP expression after the treatment of 3T3-L1 preadipocytes with CZ@LC and CZP@LC. Both CZ@LC and CZP@LC clearly exhibited time-dependent cellular transfection, and the fluorescence intensity in the CZP@LC group was slightly greater than that in the CZ@LC group (Fig. 6E–G), which might be attributed to the fact that CZP@LC has greater surface potential

and accommodates more LC plasmids than does CZ@LC, which has a stronger gene delivery capability. Consistently, flow cytometry analysis of the percentage of EGFP-positive 3T3-L1 preadipocytes treated with CZ@LC or CZP@LC revealed results similar to those described above (Fig. 6H–J). Furthermore, to validate the gene editing effect of the LC plasmid, *Lpcat3* gene quantification was performed in 3T3-L1 cells after different nanoplatform treatments. As shown in Supplementary Fig. 9A, both CZ@LC and CZP@LC clearly exhibited significant inhibition. Moreover, similar results were detected at the protein level via western blotting (Supplementary Fig. 9B, C). These
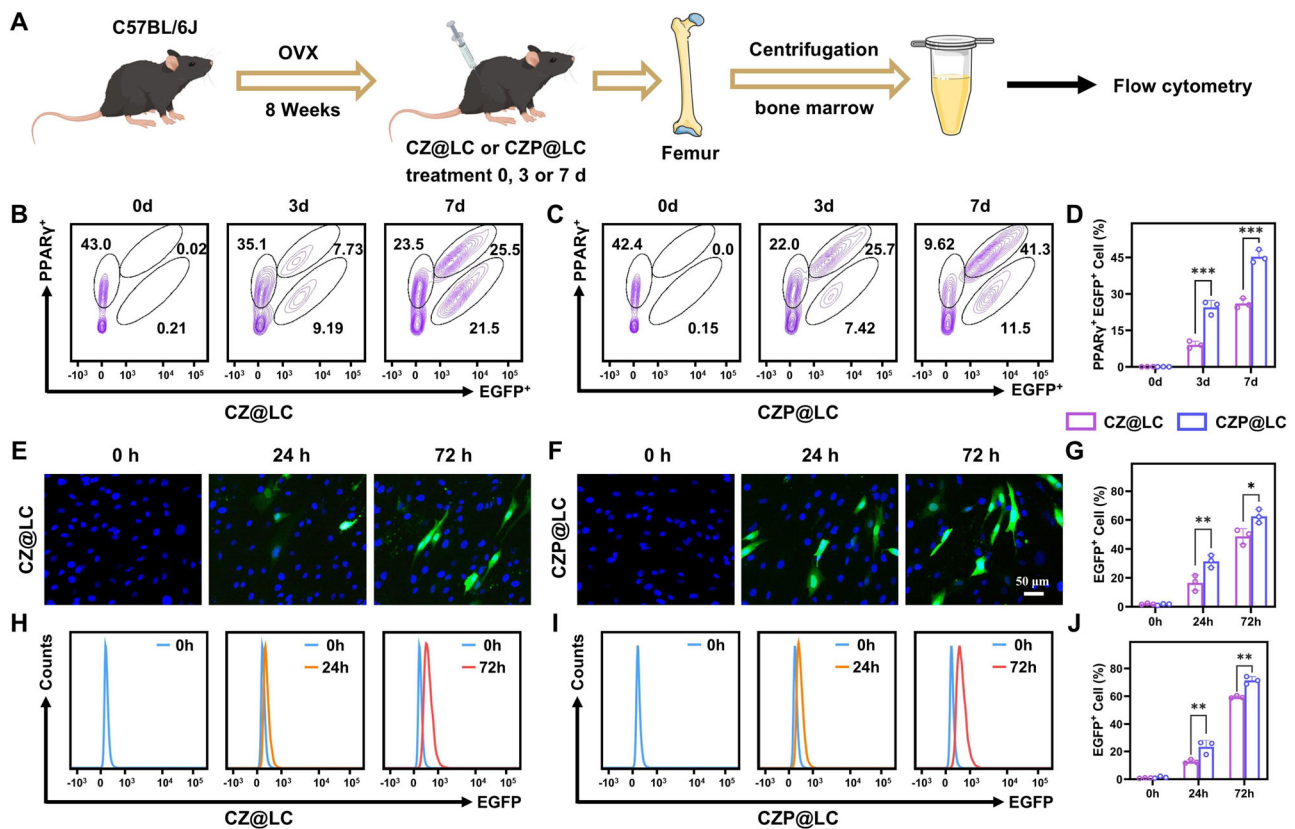
Fig. 6 | Targeting BMAds in vivo and delivery of the LC plasmid in vitro.
A Schematic diagram illustrating the experiments in which BMAds were targeted in vivo. **B–D** Flow cytometry (FCM) assessment and quantification of CZ@LC- and CZP@LC-targeted BMAds in vivo ($n = 3$ mice). **E–G** Fluorescence images and quantitative analysis of 3T3-L1 cells incubated with CZ@LC or CZP@LC for 0, 24 and 72 h ($n = 3$ independent experiments). **H–J** FCM evaluation and quantitative analysis of CZ@LC or CZP@LC uptake by 3T3-L1 cells ($n = 3$ independent experiments). The data were expressed as the means ± SDs. Statistical significance was determined by two-way ANOVA. *$p < 0.05$, **$p < 0.01$, ***$p < 0.001$. (Mouse and syringe elements from Figdraw (www.figdraw.com) are used in this figure. Microtube and femur elements adapted from Servier Medical Art (https://smart.servier.com/) are used in this figure, licensed under CC BY 4.0 (https://creativecommons.org/licenses/by/4.0/)).

results indicated that the constructed CZP@LC nanoplatforms display superior transfection ability as well as effective gene editing capability.

CZP@LC inhibits adipogenesis by interfering with lipid synthesis

As mentioned earlier, accumulated lipids lead to cellular mitochondrial dysfunction[36,37], ultimately further promoting the differentiation of BMSCs into BMAds[38]. Therefore, it is necessary to investigate whether CZP@LC could effectively interfere with lipid synthesis and thus inhibit adipogenesis. BMSCs were subjected to ADI and incubated with various nanoplatforms, and then ORO staining was utilized to assess the level of lipid synthesis and adipogenic differentiation. As shown in Fig. 7A, B, all of these nanoplatforms effectively counteracted the proadipogenic effects of ADI. Furthermore, the presence of CZP or CZP@LC resulted in smaller or single lipid droplets due to the PG3-mediated suppression of lipid synthesis. BODIPY 493/503 is a lipophilic fluorescent dye that emits bright green fluorescence when bound to neutral fats. As expected, fewer and smaller lipid droplets were observed in the PG3-carrying nanoplatform group than in the other groups (Fig. 7C, D). Moreover, the simultaneous inhibition of lipid synthesis greatly reduced lipid-induced LPO levels (Fig. 7E). The above results confirm that the levels of adipogenesis and LPO can be effectively alleviated by inhibiting lipid synthesis. Consistently, the expression of panadipocyte markers in BMAds was dramatically decreased (Fig. 7F). In addition, the primary role of adipocytes is to accumulate lipids, a process supported by the activation of lipid synthesis genes. The expression of the key adipogenic genes *Acaca*,

Fasn, *Scd1*, and *Srebf1* was blunted by PG3-carrying nanoplatform treatment during BMSC differentiation (Fig. 7G). The expression of the key genes *Dgat2*, *Lipin1* and *Gpat3*, which are crucial for triglyceride (TG) synthesis, was significantly reduced (Fig. 7H). These results indicate that CZP@LC inhibits lipid synthesis as well as LPO, thereby attenuating the adipogenesis of BMSCs. Furthermore, through immunofluorescence staining of PPARγ in mouse femur sections, PPARγ expression was significantly elevated in mice in the OVX group compared with that in the control group, and PPARγ expression was obviously suppressed in the OVX mice treated with the nanoplatforms. In particular, the mice treated with CZP@LC presented smaller and fewer BMAd vacuoles than the other groups did (Fig. 7I, J). Similarly, ORO staining revealed a similar trend among the different groups (Fig. 7K, L). These results further demonstrated that the constructed CZP@LC nanoplatforms could effectively reverse adipogenesis in OVX mice by suppressing lipid synthesis in the osteoporotic bone marrow.

CZP@LC promotes osteogenesis by restoring mitochondrial homeostasis in osteoblasts through the inhibition of lipid synthesis in adipocytes

To examine the ability of CZP@LC to rescue lipid-induced impaired osteogenic differentiation, after ADI, BMSCs were cultured with different groups of nanoplatforms in the upper transwell (TW) chamber, with MC3T3-E1 cells cultured in the lower chamber, as illustrated in Fig. 8A. Quantitative polymerase chain reaction (qPCR) analysis was performed to verify the effect of inhibited lipid synthesis by BMAds on the osteogenesis of MC3T3-E1 cells. All the nanoplatform groups
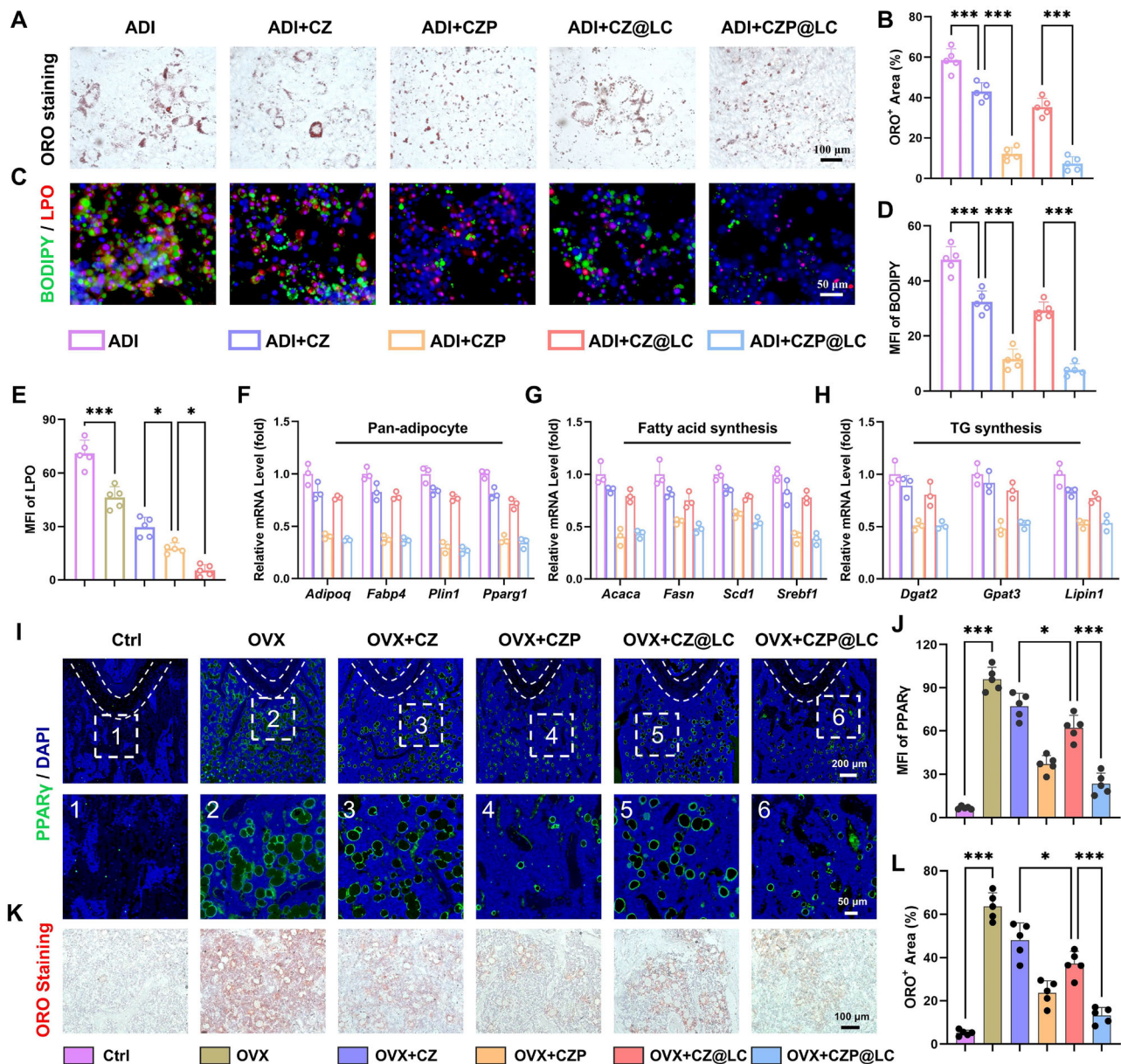
Fig. 7 | CZP@LC inhibits adipogenesis via interference with lipid synthesis in vitro and in vivo. A, B Representative images and quantification of ORO staining in BMSCs after ADI with different treatments (n = 5 independent experiments). **C–E** Representative images and quantification of BODIPY and LPO staining in BMAds subjected to different treatments n = 5 independent experiments). **F–H** qPCR analysis of gene expression in BMSCs after various ADI treatments (n = 3 independent experiments). **I, J** Immunofluorescence and quantitative analysis of PPARγ in femoral sections and enlarged images (n = 5 mice). **K, L** Representative images and quantitative analysis of ORO staining in femoral sections (n = 5 mice). The data were expressed as the means ± SDs. Statistical significance was determined by one-way ANOVA. *p < 0.05, **p < 0.01, ***p < 0.001.

presented upregulated expression of osteogenic marker genes, Ocn, Osterix (Osx), and including Runt-related transcription factor 2 (Runx2), (Fig. 8B–D). Notably, the most significant change was observed in the CZP or CZP@LC TW groups, which could be attributed to the greatest effect on lipid inhibition. The osteogenic differentiation ability of MC3T3-E1 cells was subsequently evaluated via ALP staining after 7 days of osteogenic induction culture. Compared with the ADI TW group, the CZ or CZ@LC treatment increased ALP activity in the lower chamber of the cells, and the CZP and CZP@LC groups were more effective at rescuing the ALP activity of MC3T3-E1 cells, which was attributed to the fact that they both effectively inhibited lipid synthesis in the BMAds (Fig. 8E, F). Consistently, Alizarin Red S (ARS) staining for calcium mineral deposit evaluation in MC3T3-E1 cells

produced comparable results (Fig. 8G, H). Furthermore, to further elucidate the intrinsic effects of lipids secreted by BMAds on osteoblasts, the mitochondria of MC3T3-E1 cells in the lower layer of the Transwell system were observed via TEM. The number of mitochondrial cristae in MC3T3-E1 cells in the ADI group was clearly significantly reduced, and even mitochondrial fragmentation occurred, which was slightly rescued in the CZ or CZ@LC groups, whereas the number of mitochondrial cristae (yellow arrow) was rescued in the CZP or CZP@LC groups due to robust inhibition of lipid synthesis (Fig. 8I). The Seahorse assay reflects the mitochondrial activity of cells by measuring their oxygen consumption rate (OCR); thus, MC3T3-E1 cells were cocultured with BMSCs under different conditions (Ctrl, ADI, and ADI + CZP@LC), and the OCR was detected via a Seahorse analyzer.
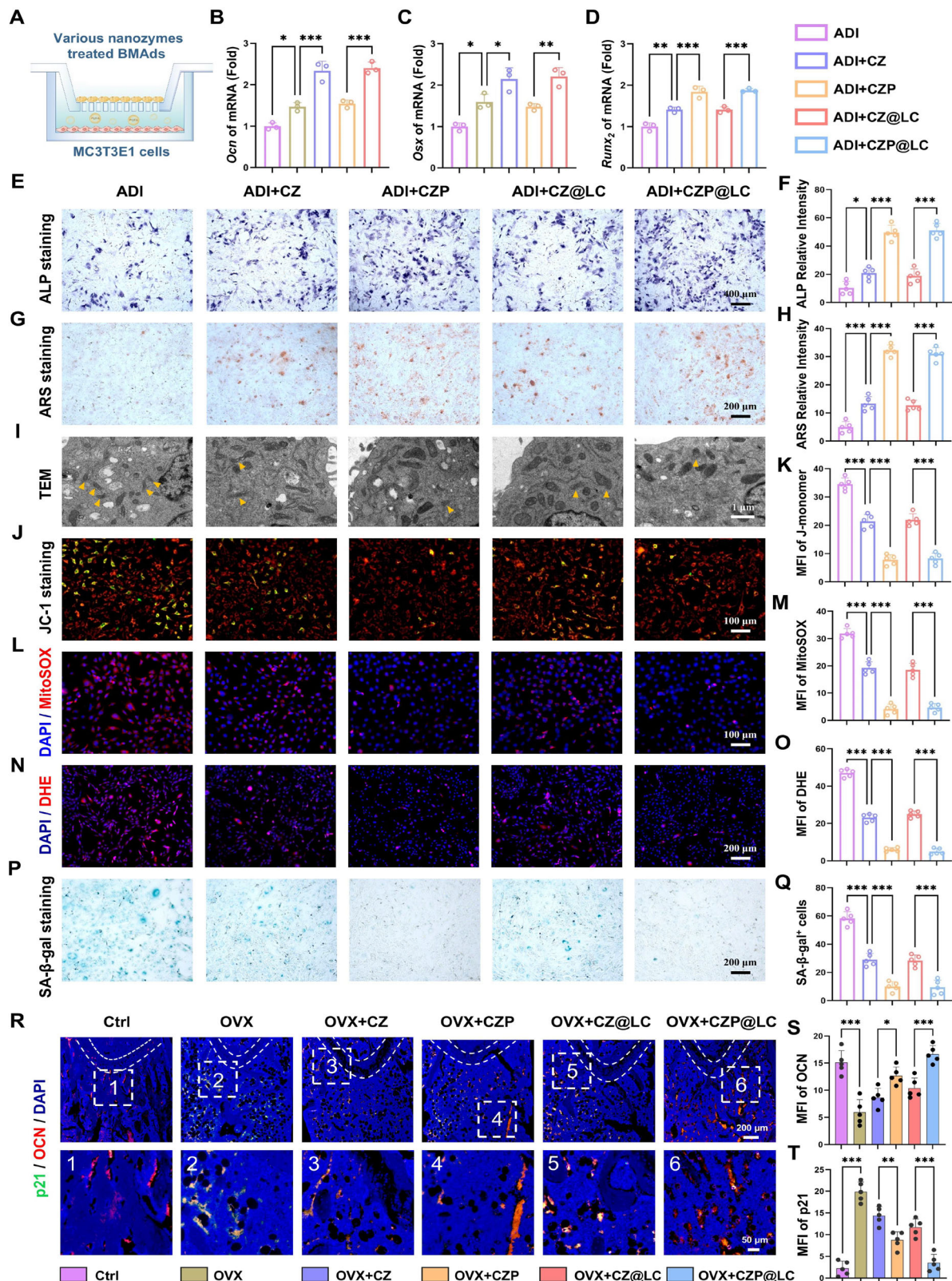
Fig. 8 | CZP@LC promote osteogenesis and protection against cellular senescence due to mitochondrial dysfunction. **A** Schematic diagram illustrating the experimental procedure. **B–D** Expression of osteogenesis-related genes (*Ocn, Osx,* and *Runx$_2$*) in MC3T3-E1 cells after different treatments (*n* = 3 independent experiments). **E–H** Representative images and quantitative analyses of ALP and ARS staining (*n* = 5 independent experiments). **I** TEM images of the effect of BMAd-generated lipids on the mitochondria of MC3T3-E1 cells (yellow arrows point to mitochondrial cristae). **J–M** Representative images and quantitative analyses of JC-1 and mitoSOX staining (*n* = 5 independent experiments). **N–Q** Images and quantification of different groups of MC3T3-E1 cells after DHE and SA-β-gal staining (*n* = 5 independent experiments). **R–T** Immunofluorescence costaining images and quantitative analysis of OCN and p21 in femoral sections (*n* = 5 mice). The data were expressed as the means ± SDs. Statistical significance was determined by one-way ANOVA. *$p < 0.05$, **$p < 0.01$, and ***$p < 0.001$.
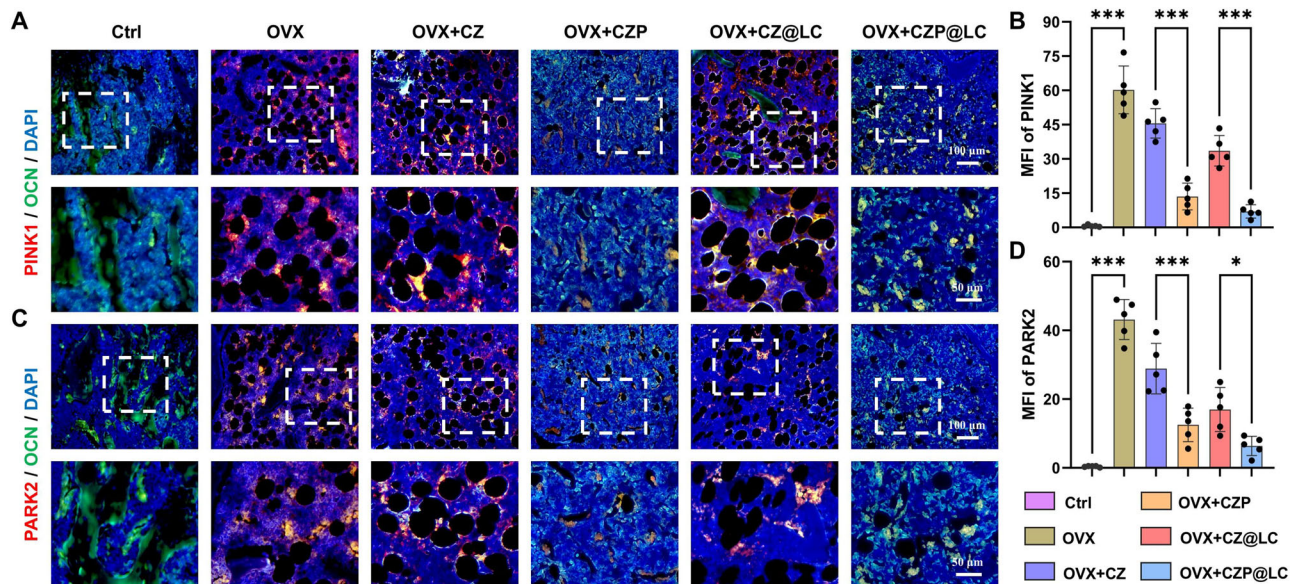
Fig. 9 | The nanoplatforms effectively rescued mitochondrial dysfunction in osteoblasts in vivo. A, **B** Levels of PINK1 and PARK2 (**C**, **D**) costained with OCN in femoral tissue and the quantitative results (*n* = 5 mice). The data were expressed as the means ± SDs. Statistical significance was determined by one-way ANOVA. *$p < 0.05$, **$p < 0.01$, and ***$p < 0.001$.

The results demonstrated that CZP@LC effectively rescued mitochondrial activity, which was attributed to the fact that CZP@LC could inhibit lipid synthesis in BMAds obtained after ADI (Supplementary Fig. 10). Next, further examination of mitochondrial function via JC-1 staining revealed that lipids secreted by BMAds significantly decreased the mitochondrial membrane potential, and this change was significantly and effectively reversed in the CZP and CZP@LC groups compared with the CZ and CZ@LC groups (Fig. 8J, K). Consistently, mitochondrial superoxide staining showed similar results (Fig. 8L, M). The DHE probe was subsequently used to detect changes in ROS levels induced by lipid-induced mitochondrial disorders in MC3T3-E1 cells. The results showed that inhibiting lipid synthesis in BMAds significantly attenuated the ROS level in MC3T3-E1 cells (Fig. 8N, O). Consequently, SA-β-gal staining revealed that the CZP@LC group had the greatest ability to rescue MC3T3-E1 cells from senescence (Fig. 8P, Q). These results suggest that excessive lipid synthesis and secretion affect mitochondrial dysfunction, leading to cellular senescence that impairs osteogenesis, and that the CZP@LC nanoplatform could significantly mitigate these detrimental effects by inhibiting lipid synthesis in BMAds.

The nanoplatforms were then injected into the femoral bone marrow cavity of OVX mice to further validate their effects on osteogenesis in vivo under high-lipid conditions. In contrast, OCN staining revealed a marked increase in the CZP and CZP@LC groups, suggesting that the inhibition of high-lipid synthesis in the OVX group effectively rescued bone formation. Furthermore, costaining of p21 with OCN markedly reduced the number of senescent osteoblasts in the CZP@LC group compared with that in the OVX group, indicating that osteoblast senescence in osteoporotic bone marrow was rescued (Fig. 8R–T), which resulted from the inhibition of lipid synthesis as well as ROS. These findings confirmed that CZP@LC can rescue mitochondrial dysfunction by inhibiting lipid synthesis, thereby alleviating cellular senescence and promoting osteogenesis.

Furthermore, to verify the specific mechanism of mitochondrial impairment caused by lipids in osteoblasts, BMAds were obtained from BMSCs under ADI conditions and cocultured with MC3T3-E1 cells. The PPARγ antagonist GW9662 was subsequently used to alleviate MC3T3-E1 cells after ADI, which was confirmed by JC-1 and MitoSOX staining. In addition, treatment of ADI-conditioned BMAds with CZP@LC rescued mitochondrial dysfunction in MC3T3-E1 cells, which reappeared after the addition of the PPARγ agonist GW1929 (Supplementary Fig. 11A–D). Consistently, the upregulation of PINK1 and PARK2 expression suggested that mitochondrial dysfunction was also reversed after CZP@LC treatment and upregulated again after GW1929 treatment (Supplementary Fig. 11E–H). Moreover, immunofluorescence costaining of femoral sections for PINK1, PARK2 or OCN revealed that the inhibition of lipid synthesis effectively rescued mitochondrial dysfunction (Fig. 9A–D). These results suggest that lipids influence mitochondrial dysfunction in osteoblasts through the PPARγ signaling pathway.

Biosafety and off-target evaluation of CZP@LC in vivo

The major organs and blood biochemistry of the mice were examined within 30 days of administration to assess the biosafety of CZP@LC. The findings indicated that there were no statistically significant differences in hematological parameters (such as leukocytes, erythrocytes, and platelets), hepatic biochemical indicators (including alanine aminotransferase, alanine transaminase, total protein, albumin, and total bilirubin), or renal biochemical markers (creatinine and blood urea nitrogen) between the treatment and control groups (Supplementary Fig. 12A). Moreover, after the administration of CZP@LC, the heart, liver, spleen, lungs, and kidney were removed and stained with hematoxylin–eosin for histological evaluation at different time points (1, 3, 7, 14, and 30 days). The results revealed that the morphologic structures of these organs all remained normal, which was consistent with the physiologic state, and no obvious inflammation or necrosis was observed, similar to the situation in mice before injection (Supplementary Fig. 12B). Furthermore, to elucidate the impact of prolonged inhibition of lipid synthesis in BMAds on other physiological functions, hepatic and renal functions in mice were evaluated following a 2-month administration of CZP@LC. The results indicated that the suppression of lipid synthesis in BMAds did not significantly affect the functionality of other organs within the organism (Supplementary Fig. 13A–F).

Furthermore, to investigate the in vivo distribution and metabolic properties of CZP@LC, we successfully prepared Ce6-CZP@LC. We

subsequently performed ex vivo fluorescence imaging of the major organs of the mice at different time points (0, 24, 48, and 72 h) after the injection of Ce6-CZP@LC, and the nanoplatform clearly exhibited strong fluorescence in the bone marrow for more than 72 h, with metabolic clearance predominantly occurring via the liver and kidneys (Supplementary Fig. 13G). In addition, the expression levels of *Lpcat3* in different organs were analyzed via qPCR to evaluate potential off-target effects. The results revealed that there was no significant change in the expression level of *Lpcat3* in off-target organs, which indicated that the CZP@LC nanoplatform has favorable biosafety (Supplementary Fig. 14A). Moreover, to evaluate the potential compensatory effect of BMAds, BMAds were obtained after the induction of adipogenesis in BMSCs, which were then treated with CZ, CZP, CZ@LC, or CZP@LC. Their homologous genes (e.g., *Lpcat1* and *Lpcat2*), as well as *Mfsd2a*, which is responsible for lipid transport, were quantified via qPCR[39]. As a result, no compensatory upregulation of *Lpcat1* or *Lpcat2* occurred, and the upregulation of *Mfsd2a* may compensate for the loss of ara-chidonoyl phospholipids (Supplementary Fig. 14B). These results collectively substantiate the high biosafety and biocompatibility of the CZP@LC nanoplatform.

CZP@LC restored osteoporotic bone marrow homeostasis by inhibiting lipid metabolism

To explore the superior osteoprotective properties of these nano-platforms in vivo, the mice were subjected to sham surgery or OVX. The nanoplatforms were subsequently locally administered into the bone marrow cavity of the femur. No adverse effects or mortality were observed in any of the mice. The animals were euthanized, and the femurs were harvested 8 weeks post-OVX for further analysis. µCT scanning and subsequent reconstruction revealed that bone mass was greater in OVX mice treated with alendronate than in those treated with various nanoplatforms. Compared with those in the CZP group, the bone mass of the mice in the alendronate group was improved, but the bone mass recovery was significantly greater in the CZP@LC group than in the alendronate group (Fig. 10A). Consistent with these findings, histologic examination (HE staining) revealed that the number of vacuoles indicative of BMAds in the CZP and CZP@LC groups was significantly lower than that in the OVX, CZ and CZ@LC groups (Fig. 10B). Further analysis of µCT of the corresponding bone parameters revealed that bone volume per tissue volume (BV/TV), trabecular thickness (Tb.Th), and trabecular bone number (Tb.N) were greater in the CZP and ALN groups than in the OVX group, whereas trabecular separation (Tb.Sp) was lower. Furthermore, the alterations in bone parameters were significantly greater with CZP@LC than with both CZP and alendronate (Fig. 10C–F). In addition, to further validate the therapeutic potential of these nanoplatforms in an established osteo-porosis model, these nanoplatforms were injected into the femurs of mice 6 weeks after OVX to verify their therapeutic effects. As expected, CZP@LC still promoted robust bone regeneration by inhibiting lipid synthesis and rescuing the collapsed bone marrow microenvironment (Supplementary Fig. 15A). In contrast, after CZP@LC treatment, the trabecular structure was dense and uniform, and the intertrabecular connections were complete and clear (Supplementary Fig. 15B). HE staining of the femoral tissue revealed that the OP (established osteoporotic model) group exhibited sparse trabeculae, thin trabe-culae, and wider spacing between trabeculae (Supplementary Fig. 15C). Furthermore, immunofluorescence analysis of femoral sections confirmed that, compared with the OP group, the CZP@LC group pre-sented increased bone formation and a reduced presence of BMAds (Supplementary Fig. 15D–G). These results confirm that the inhibition of lipid synthesis is a promising therapeutic modality for osteoporosis.

In addition, we aimed to further validate the therapeutic effect of the nanoplatforms on osteoporosis caused by obesity-induced abnor-mal accumulation of adipocytes in the bone marrow cavity. Mice fed a high-fat diet (HFD) for 8 weeks were treated with CZ, CZP, CZ@LC, or CZP@LC, and the femurs were harvested for µCT. Bone reconstruction revealed that both CZP and CZP@LC, which carry PG3, improved the bone loss caused by the HFD (Supplementary Fig. 16A). Moreover, bone parameter analysis also revealed a consistent salvage effect (Supplementary Fig. 16B). Histological HE staining of the femur substantiated the therapeutic efficacy of these nanoplatforms. Notably, CZP and CZP@LC demonstrated significant therapeutic effectiveness, attributed to their capacity to inhibit lipid synthesis in BMAds (Supplementary Fig. 16C). Femoral immunofluorescence analysis of OCN and PPARγ consistently revealed that CZP@LC significantly promoted osteogenesis while concurrently suppressing adipogenesis (Supplementary Fig. 16D–G). These results suggest that CZP@LC, which aims to suppress lipid synthesis in BMAds and eliminate ROS in the microenvironment, is a promising innovative therapeutic approach for modulating the bone marrow microenvironment and restoring bone homeostasis.

Discussion

With age, BMSCs tend to differentiate into BMAds rather than osteoblasts, which contributes to a progressive decline in bone mass and an accumulation of BMAds within the bone marrow cavity[26]. These increased BMAds in the bone marrow cavity may be involved in the pathogenesis of osteoporosis through the secretion of various cytokines, such as RANKL, SASP, and leptin[40]. However, the effects of lipids secreted by BMAds on the microenvironment and other cellular entities remain largely unexplored. In this study, an osteoporosis model was established to screen for significantly altered lipid AA via lipidomic analysis. Subsequent in vitro cellular experiments further demonstrated that lipid accumulation modifies the differentiation propensity of BMSCs toward adipogenesis while concurrently accelerating cellular senescence through the disruption of mitochondrial functional homeostasis in adjacent cells, thus playing a critical role in the progression of osteoporosis. Therefore, altering the aberrant metabolic state induced by the bone microenvironment through the modulation of lipid synthesis may offer an additional perspective for the development of targeted therapies for bone loss.

PG3 has been reported to be selectively distributed in adipose tissue because of its cationic surface properties and to reduce lipid synthesis or accumulation by influencing metabolic pathways[41]. However, this inhibition is not complete, and some lipids are still oxidized by LPCAT3, leading to LPO-promoted adipogenesis. Therefore, the addition of the LC plasmid to PG3 may serve as a complementary strategy to further inhibit adipogenesis. Moreover, our results indicate that even if lipid synthesis and LPO production are inhibited, ROS in the bone marrow microenvironment may interfere with the therapeutic effect. To overcome the adverse effects of microenvironmental ROS on the regulation of lipid metabolism[42], Cu-doped ZIF8 was chosen as a carrier for PG3 loaded with the LC plasmid owing to its marked antioxidant effect and high porosity[24]. Accordingly, CZP@LC nanoplatforms formed by CZ encapsulation of PG3@LC interfere with lipid synthesis in BMAds while modulating the bone microenvironment, thereby inhibiting lipid crosstalk between BMAds and other cells to remodel bone formation.

Hopefully, both in vitro and in vivo, CZP@LC will be more efficiently transfected and effectively targeted to BMAds. More importantly, the incorporation of nanoplatforms containing PG3 components into the induction of adipogenesis in BMSCs significantly inhibited lipid synthesis. In the transwell coculture system involving BMAds and MC3T3-E1 cells, lipids secreted by BMAds impaired the osteogenic differentiation of MC3T3-E1 cells. This impairment was substantially ameliorated by the administration of CZP or CZP@LC, which may be attributed to the marked inhibition of abnormal lipid metabolism by CZP@LC, which protected mitochondria from dysfunction and facilitated osteoblast differentiation and function. Overall, a beneficial cascade effect on bone homeostasis may be achieved by interfering with lipid synthesis and the inhibition of microenvironmental ROS.
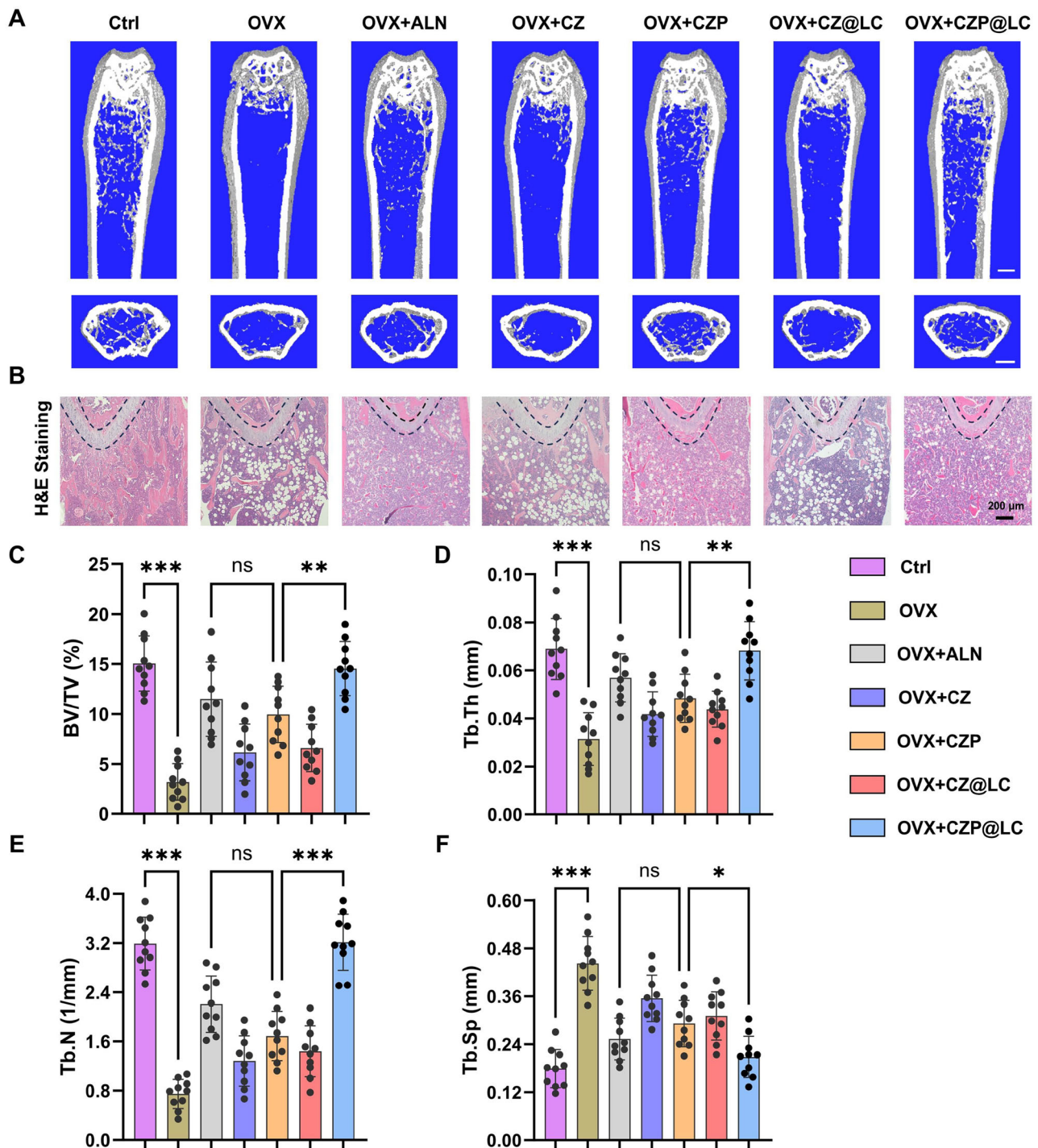
Fig. 10 | CZP@LC reverses osteoporotic bone loss in vivo. A Representative μCT image of femurs (scale bars: 0.5 mm). **B** Images obtained from HE staining indicated that more bone microstructures were maintained and that fewer fat vacuoles were present in the CZP@LC-treated OVX mice. **C–F** Quantitative μCT analysis of BV/TV, trabecular thickness (Tb. Th), trabecular number (Tb. N) and Tb. Sp ($n = 10$ mice). The data were expressed as the means ± SDs. Statistical significance was determined by one-way ANOVA. $*p < 0.05$, $**p < 0.01$, and $***p < 0.001$.

In summary, the excessive adipogenic differentiation and subsequent abnormal lipid metabolism observed in osteoporosis significantly contribute to malignant mitochondrial function, exacerbating the senescence of normal cells. Furthermore, the accumulated PUFAs and compromised microenvironment can further weaken osteogenesis while enhancing adipogenesis, thereby perpetuating a deleterious feedback loop. On this basis, the constructed CZP@LC nanoplatform remodeled the bone microenvironment by targeting BMAds and protected cells from mitochondrial dysfunction by interfering with aberrant lipid metabolism, thus providing an innovative targeted biotherapeutic strategy for osteoporosis from a cellular lipid metabolism perspective.

Methods

Ethical statement

All animal procedures were conducted in strict compliance with protocols approved by the Ethics Review Committee of Animal Experimentation at Yangzhou University (No. 202412013). These procedures

were conducted in accordance with the guidelines set forth in the National Institutes of Health's Guide for the Care and Use of Laboratory Animals and in compliance with the principles of the Animal Welfare Act.

Materials, cell lines, and animals

3T3-L1 (iCell-m066) and MC3T3-E1 (iCell-m031) cell lines were procured from iCell Bioscience (Shanghai, China), and BMSCs and BMMs were isolated from C57/B6J mice. The cells were maintained in either Dulbecco's Modified Eagle's Medium (DMEM) or Minimum Essential Medium Alpha (MEM-α), both supplemented with 10% fetal bovine serum, as well as 1% penicillin and streptomycin. $Zn(NO_3)_2 \cdot 6H_2O$ (228737) and PG3 (412422) were purchased from Sigma–Aldrich, and $Cu(NO_3)_2 \cdot 3H_2O$ (C140879) and 2-methylimidazole (M104839) were obtained from Aladdin. The cells were cultured in an incubator set to 37 °C with a 5% CO_2 atmosphere. Eight-week-old female and male C57BL/6J mice were procured from the Comparative Animal Center Laboratory at Yangzhou University in Yangzhou, China. The mice were housed in sanitized isolators within the animal facility, with a maximum of six mice per cage. Water was freely available, and the mice were subjected to a light–dark cycle of 12 h per day (from 7 a.m. to 7 p.m.) while being housed at a constant temperature of 25 °C. All animal experiments were performed following the ethical protocol approved by the Institutional Committee for Animal Protection and Use at Yangzhou University. The LC plasmid was synthesized by GenePharma (Shanghai, China), and its sequence is illustrated in Supplementary Fig. 17.

Instruments

The morphology and particle size of all the nanoplatforms were examined via TEM. EDS can be used to determine the elemental composition of the final nanoplatform, and element mapping represents the distribution of the elements. The sizes of all the nanoplatforms and the potential of each component were analyzed via a Zetasizer (Malvern, UK). The elemental composition was further examined via XPS (Thermo Scientific, ESCALAB 250Xi, USA), and XRD (D8 Advance, Germany) was employed for structural characterization. FT-IR spectra were acquired via a micro infrared spectrometer (670-IR + 610-IR; Varian, Palo Alto, CA) over the spectral range of 400–4000 cm^{-1}. For ICP (PerkinElmer Elan, DRC-e, USA), 10 mg of CZP@LC was dissolved in an acidic solution at pH 6.0, and the concentration of metal particles in the solution was examined at different time intervals. The lipid analysis through liquid mass spectrometry (Jasper HPLC). The OCR were obtained from a Seahorse XFe24 Analyzer (Agilent Technologies, USA). Ex vivo fluorescence imaging of organs was examined by Small Animal Optical Imaging System (IVIS Lumia III, PerkinElmer, USA).

Synthesis of CZ, CZP, and CZ@LC

For CZ synthesis, the following steps were used: $Zn(NO_3)_2 \cdot 6H_2O$ (297.49 mg, 1 mmol) and 1.0 mmol of $Cu(NO_3)_2 \cdot 3H_2O$ (187.56 mg, 1 mmol) were dissolved in a three-necked flask containing 10 ml of DEPC water with stirring for 10 min. To synthesize CZP or CZ@LC, PG3 (690.88 mg, 0.1 mmol) or 300 µg of LC plasmid was added at this point, and the mixture was stirred for 20 min. Then, 10 mL of DEPC water containing 2-methylimidazole (656.80 mg, 8 mmol) was added dropwise, and the mixture was stirred continuously for 24 h. The above mixture was collected in a centrifuge tube by centrifugation at 9000×g for 10 min, and the supernatant was discarded to collect the precipitate. The samples were washed three times with water and finally resuspended in DEPC water for further use.

Preparation of PG3@LC, CZP@LC, and Ce6-CZP@LC

Initially, the LC plasmid was incubated with different ratios of PG3 at 4 °C for 24 h to facilitate the piggyback of the plasmid onto PG3. Next,

the optimal loading efficiency was determined by 10% agarose gel electrophoresis at 118 V for 50 min. Next, to synthesize CZP@LC, $Zn(NO_3)_2 \cdot 6H_2O$ (297.49 mg, 1.0 mmol) and $Cu(NO_3)_2 \cdot 3H_2O$ (241.60 mg, 1.0 mmol) were subsequently dissolved in 10 ml of DEPC water and stirred for 10 min, after which the PG3 and LC plasmid mixtures previously prepared at the optimal ratio were added and mixed for 20 min. A solution containing 2-methylimidazole (656.8 mg, 8.0 mmol) was subsequently added dropwise, and the mixture was stirred for 24 h. Then, the precipitate was collected at 9000×g for 10 min and washed three times with water. Finally, it was resuspended in DEPC water and stored at 4 °C until further use.

Ce6-PG3@LC was prepared by reacting the amino group on the surface of PG3@LC obtained above with Ce6 via an amination reaction to form an amide bond. Next, as above, $Zn(NO_3)_2 \cdot 6H_2O$ and $Cu(NO_3)_2 \cdot 3H_2O$ were dissolved in DEPC water with stirring for 10 min, Ce6-PG3@LC was added, and the mixture was stirred for 20 min. Subsequently, dimethylimidazole was added to continue the reaction for 24 h. The resulting product was washed and centrifuged to obtain Ce6-CZP@LC.

SOD and CAT-like activities and •OH scavenging ability

The superoxide anion ($\bullet O_2^-$) scavenging activity of the CZP@LC nanoplatform was evaluated via a SOD enzyme activity kit (SOD-1-Y, Cominbio, China). The detection method involved the generation of superoxide anions ($\bullet O_2^-$) through the reaction of xanthine and xanthine oxidase, resulting in the reduction of nitroblue tetrazolium to formazan, which exhibited strong absorption at 560 nm. Superoxide dismutase was able to neutralize $\bullet O_2^-$ and prevent the formation of formazan. A reduction in the intensity of the blue coloration within the reaction mixture signifies an increase in SOD activity.

CAT activity can be evaluated by quantifying the oxygen concentration in the solution following the reaction between CZP@LC and H_2O_2 via a dissolved oxygen meter (Lightning Magnetic, JPSJ-606 L, China).

The hydroxyl radical (•OH) scavenging activity of CZP@LC was evaluated via an •OH scavenging capacity assay kit (BC1325, Solarbio, China) following the manufacturer's protocol. The underlying principle of the assay is as follows: hydroxyl radicals generated via the Fenton reaction between H_2O_2 and Fe^{2+} oxidize Fe^{2+} to Fe^{3+}, leading to a reduction in the absorbance at 536 nm. The extent of hydroxyl radical scavenging is indicated by the inhibition of the rate of decrease in the absorbance at this wavelength.

Bone marrow lipidomic analysis

Mouse femurs were harvested 8 weeks after sham surgery or OVX (n = 6 mice respectively), after which the bone ends were cut. Then, the bones were transferred to a 0.6 mL microcentrifuge tube. The bone-containing small tube was then inserted into a 1.5 mL microcentrifuge tube, and fresh bone marrow was extracted via rapid centrifugation. Erythrocytes were lysed with erythrocyte lysis buffer, and the remaining cells were centrifuged (4500×g, 5 min, RT). The floating adipocytes and lipids were collected from the supernatant, rinsed twice with PBS, and then sent to Hangzhou Cosmos Wisdom Biotech Co., Ltd., for widely targeted lipidomic analysis. Briefly, metabolites were extracted via methanol, followed by the addition of methyl tert-butyl ether for lipid extraction. Then, a stratified liquid surface with lipids in the upper layer and water-soluble metabolites in the lower layer was obtained after centrifugation at 9000 × g for 10 min. Next, an equal amount of the upper organic phase was taken for lipid analysis via liquid mass spectrometry (Jasper HPLC). The mobile phase consisted of two solutions: Phase A (50% water, 50% acetonitrile, 10 mmol L^{-1} ammonium formate) and Phase B (10% acetonitrile, 88% isopropanol, 2% water, 10 mmol L^{-1} ammonium formate). A gradient elution was used: 0–0.5 min at 20% B, 4 min at 70% B, 10–12 min at 99% B, 12.1–15 min at 20% B. The flow rate was 0.4 mL min^{-1}, column

temperature 50 °C, sample tray 10 °C, and injection volume 2 µL. Mass spectrometry was performed with a 4500 or 6500 triple quadrupole, optimizing deprotonation potential and collision energy for lipid classes. Additional parameters: IS 5200/-4500, TEM 500, CUR 35, GS1 55, GS2 55, controlled by Analyst 1.6 software.

Isolation of primary BMSCs
Eight-week-old C57/B6J mice were euthanized and sterilized with 75% alcohol for 5 min. Then, the femur was removed, the ends were removed, and the bone marrow was centrifuged at 2500×g for 3 min in EP tubes. Erythrocytes were removed from the bone marrow with erythrocyte lysate and centrifuged again, after which the cells were resuspended in MEMα supplemented with 10% fetal bovine serum, 1% penicillin, and streptomycin. Finally, the resuspension was placed in a 100 mm dish and cultured, and the adherent cells were considered BMSCs after 12 h.

Enzyme-linked immunosorbent assay (ELISA) of AA
To assess the levels of AA in the femurs of OVX mice, femurs were harvested at various weekly intervals post-OVX. The collected femurs were weighed, sectioned, and homogenized by grinding in PBS supplemented with protease inhibitors on ice. The homogenate was subsequently centrifuged at 7000 × g for 10 min at 4 °C. The resulting supernatant was then utilized to quantify the AA levels via a commercial assay kit (E-EL-0051, Elabscience, China) in accordance with the manufacturer's protocol.

Fatty acid antagonist and agonist experiments
BMAds were obtained from BMSCs through ADI and subsequently cocultured with MC3T3-E1 cells to assess the impact of lipids on MC3T3-E1 cells, and the coculture groupings were as follows: Ctrl (BMSCs without ADI), Ctrl+GW1929 (HY-15655, MedChemExpress, China), ADI and ADI + GW9662 (HY-16578, MedChemExpress, China). PINK1 (sc-518052, Santa Cruz Biotechnology, USA) and PARK2 (66674-1-Ig, Proteintech, USA) immunofluorescence and JC-1 (C2006, Beyotime, China) and MitoSOX (HY-D1055; MedChemExpress, USA) staining were subsequently used to assess mitochondrial dysfunction in MC3T3-E1 cells.

In vitro cell viability analysis
MC3T3-E1 cells were cultured in 96-well plates and exposed to various concentrations of synthesized nanoplatforms at 37 °C and 5% CO$_2$ for 24 h. Subsequently, 10% CCK-8 (BS350A, Biosharp, China) reagent was added, and the mixture was incubated for 40 min, after which the absorbance at 450 nm was measured via an enzyme marker.

Assessment of mitoSOX, ROS, cellular senescence, or the SASP in vitro
The cellular levels of mitochondrial superoxide and ROS were evaluated with mitoSOX Red, JC-1 and DHE probes (S0064S; Beyotime, China), respectively, following the manufacturers' protocols. MC3T3-E1 cells were cultured in six-well plates with 20 µM arachidonic acid and treated with various nanoplatforms for 24 h. Subsequently, the cells were washed three times with PBS before being subjected to mitoSOX or DHE staining for 30 min and finally labeled with DAPI for 5 min. The resulting red fluorescence was then visualized via a fluorescence microscope.

The senescence of MC3T3-E1 cells was evaluated via a SA-β-gal staining kit (C0602, Beyotime, China). MC3T3-E1 cells subjected to various treatments were cultured in 6-well plates. After three washes with PBS, the cells were fixed for 15 min and then incubated with SA-β-gal staining solution at 37 °C overnight. Finally, random imaging was conducted to identify SA-β-gal-positive cells, which were stained blue.

SASP expression was assessed via immunofluorescence in cocultured cells by washing with PBS, fixing with 4% paraformaldehyde, permeabilizing with 0.1% Triton X-100 in PBS, blocking with 5% bovine serum albumin, and incubating with anti-TNFα (80258-6-RR, Proteintech, USA) or IL-1β (ab315084, Abcam, UK) primary antibodies overnight at 4 °C. The cells were subsequently incubated with Alexa Fluor® 488- or 594-conjugated secondary antibodies for 2 h at room temperature, and the nuclei were stained with DAPI for 5 min. The final observation was conducted via fluorescence microscopy.

Cellular internalization through confocal laser scanning microscopy (CLSM) and flow cytometry (FCM)
To validate the targeting ability of BMAds in vivo, the bone marrow cavities of mice 8 weeks after sham operation or OVX were injected with CZ@LC or CZP@LC, and the femurs were harvested after 0, 3, and 7 days. After the ends of the femur were cut and placed in an EP tube, the bone marrow was centrifuged, and the adipocytes were labeled with PPARγ (sc-271392 PE, Santa Cruz Biotechnology, USA)[43,44] or CAV-1 (sc-70516 PE, Santa Cruz Biotechnology, USA) and then FCM-sorted to identify the PPARγ$^+$EGFP$^+$ or CAV-1$^+$EGFP$^+$ cell population.

The cellular internalization of the nanoplatform was evaluated via confocal laser scanning microscopy (CLSM) and flow cytometry (FCM). 3T3-L1 cells (5 × 10^4/well) were seeded in 12-well plates and treated with either 100 µg ml^{-1} CZ@LC or CZP@LC. The cells were subsequently cultured for 24 and 72 h. Expression of the LC plasmid resulted in green fluorescence. Nuclei were stained with DAPI for 1 min, followed by three washes with PBS. The cells were then examined via CLSM (Leica, TCS SP5, Germany). Alternatively, the cell suspension could be directly collected for analysis via a flow cytometer. The gating strategy used for flow cytometric data is shown in Supplementary Fig. 18.

Western blot
3T3-L1 cells were subjected to various treatments: Ctrl, CZ, CZP, CZ@LC, or CZP@LC for 72 h. Then, the cells were subjected to rapid lysis via cell lysis buffer (P0013, Beyotime, China), followed by protein quantification via BCA protein assay kits (P0012, Beyotime, China). The extracted proteins were subsequently analyzed through gel electrophoresis and transferred onto nitrocellulose membranes (FFN08, Beyotime, China). The membranes were then blocked with a 5% solution of bovine serum albumin for 1 h and subsequently incubated with primary antibodies at 4 °C overnight. After three washes and incubation with HRP-conjugated secondary antibodies, the immunoblots were detected via a chemiluminescence kit (P10100, NCM Biotech, China) and subsequently visualized via an automated chemiluminescence image analysis system (Tanon, China). Western blotting was conducted with the following antibodies: β-actin (66009-1-Ig, Proteintech, USA) and LPCAT3 (67882-1-Ig, Proteintech, USA).

Seahorse assay
The OCR was assessed via the Seahorse XFe24 Analyzer (Agilent Technologies, USA) in conjunction with the Seahorse XF Cellular Mitochondrial Stress Test Kit (103015-100; Agilent Technologies, USA) according to the manufacturer's protocol. Briefly, MC3T3-E1 cells cocultured with different groups of BMAds were seeded at a density of 5 × 10^4 cells per well in 24-well Seahorse assay plates and incubated overnight at 37 °C to facilitate adherence. The cells were moistened twice with seahorse-specific test medium and incubated in a non-CO$_2$ incubator for 1 h. Subsequently, distinct respiratory chain inhibitors were sequentially introduced at specified intervals and analyzed via an instrument.

Adipocyte differentiation and Oil Red O, BODIPY, and LPO staining
The BMSCs underwent differentiation in the conventional adipogenic cocktail following the attainment of confluence for a period of 2 days. The mixture consisted of Dulbecco's Modified Eagle Medium supplemented with 10% fetal bovine serum, 1 µM dexamethasone, 10 µg mL^{-1}

insulin, and 0.5 mM 3-isobutyl-1-methylxanthine. In addition, 5 µM rosiglitazone was used during the initial two days to promote the differentiation of the BMSCs. Following the induction period, the cells were subsequently cultured in complete medium supplemented with 2.5 µg ml⁻¹ insulin until they reached full differentiation, after which the synthesized nanoplatforms were added at specified time points.

For ORO staining, differentiated adipocytes were gently washed three times with PBS before being fixed in 4% formalin buffer for 20 min. Subsequently, the cells were washed twice with water, treated with 60% isopropanol for 5 min, and stained with a freshly prepared and filtered 60% oil red O isopropanol solution for 15 min. Finally, the cells were rinsed with distilled water and imaged. The BODIPY 493/503 Staining Kit (C2053S) and LPO Assay Kit (S0043M) were obtained from Beyotime, and according to the manufacturer's instructions, differentiated adipocytes were stained and then imaged via fluorescence microscopy.

Assessing the impact of lipids secreted by BMAds on the osteogenic potential of osteoblasts

To verify the effect on the osteogenic differentiation ability of osteoblasts, BMAds differentiated from BMSCs were cultured in transwell chambers (0.4-µm pore size) with different nanoplatforms. MC3T3-E1 cells were subsequently cultured and cocultured with osteogenic induction medium. The MC3T3-E1 cells were removed after 7 days, washed with PBS and fixed with 4% paraformaldehyde for 15 min. Osteogenic differentiation activity was detected with an alkaline phosphatase stain kit (P0321S, Beyotime, China). Similarly, staining was conducted via Alizarin Red S solution (G1450, Solarbio, China) following a 21-day period of culture.

Electron microscopy

The cells were fixed in 2.5% glutaraldehyde (pH 7.4) for 2 h. After fixation, the samples were washed three times with 0.1 M phosphate buffer (pH 7.2) and subsequently fixed in 1% osmium tetroxide at 4 °C for 2 h. The samples were then subjected to dehydration through a graded series of ethanol concentrations. Following dehydration, the samples were infiltrated with Epon-Araldite resin and subsequently positioned in a mold for polymerization. Semithin sections were prepared for positioning, followed by the preparation and collection of ultrathin sections for microstructural analysis. The sections were counterstained with 3% uranyl acetate and 2.7% lead citrate, followed by examination via a Hitachi HT 7800 transmission electron microscope.

Gene expression analysis

Total RNA was extracted via TRIzol Reagent (R401-01, Vazyme, China) and subsequently quantified via a P100/P100 + DNA/Proteins Analyzer (Pultton). Here, 1 µg of total RNA was used for reverse transcription to generate complementary DNA (cDNA) via HiScript II Q RT SuperMix (R222-01, Vazyme, China) in accordance with the manufacturer's instructions. The resulting cDNA was utilized for subsequent qPCR analysis. Real-time PCR was performed in a 20 µL mixture consisting of 10 µL of ChamQ Universal SYBR qPCR Master Mix (Q711-02, Vazyme, China), 1 µL of forward primer, 1 µL of reverse primer, 6 µL of DEPC water, and 2 µL of cDNA template, with the primer sequences detailed in Supplementary Table 1.

Biosafety and metabolism of nanoplatforms in vivo

The blood, heart, liver, spleen, lungs, and kidneys of 8-week-old C57BL/6J mice were collected at intervals of 1, 3, 7, 14, and 30 days following the administration of CZP@LC. The blood biochemistry, complete blood count, and HE staining of the organs were subsequently conducted to assess the biosafety of the nanoplatforms.

To evaluate the metabolism of the nanoplatforms, CZP@LC nanoplatforms were injected into the bone marrow cavities of the mice 8 weeks after OVX. Major organs and femurs were harvested at 8-, 24-, 48-, and 72-h intervals for fluorescence detection via a small animal optical imaging system (IVIS Lumia III, PerkinElmer, USA). Additionally, the bone marrow cavities of the 24-, 48-, and 72-h femurs were flushed, and BMAds and non-BMAds were separated by centrifugation. The cellular precipitates were resuspended in an amount of liquid equal to that of the supernatant and subsequently transferred to a 24-well plate for fluorescence detection.

OVX-induced osteoporosis mouse model, treatment, micro-CT scanning, and analysis

An osteoporosis model was established via sham surgery or OVX in 8-week-old C57BL/6J mice[45], followed by different treatments via femoral bone marrow cavity injections every 2 weeks for 8 weeks after surgery. For the established osteoporosis model, treatment was started 6 weeks after OVX. The mice were divided into control, OVX, OVX + CZ, OVX + CZP, OVX + CZ@LC, and OVX + CZP@LC groups ($n = 5$). Femurs were collected after the humane sacrifice of the mice at the end of the treatment and fixed in 4% paraformaldehyde for 24 h. High-resolution micro-CT (SkyScan1176, SkyScan, Atcella, Belgium) bone scans of the mouse femurs were performed with the following scan settings: 65 kV, 385 mA, and 0.5 mm Al filter, and the corresponding bone parameters were quantitatively compared and analyzed via three-dimensional reconstruction. After micro-CT analysis, the femurs were decalcified in 10% EDTA for 10 days at ambient temperature. The femur was subsequently embedded, sectioned at a thickness of 4 µm, and stained with HE, DHE, TRAP, ORO, and immunofluorescence techniques. Positive staining was assessed via fluorescence microscopy.

HFD-induced osteoporosis mouse model

Thirty male C57BL/6 J mice aged 8 weeks were divided into Ctrl, HFD, and HFD + different nanoplatform treatment groups. The control group was fed a standard diet, while the experimental group was fed an HFD. After an eight-week feeding regimen, the HFD group received various nanoplatform treatments, specifically CZ, CZP, CZ@LC, and CZP@LC, over an additional 8-week period. The femurs were subsequently harvested and fixed in 4% paraformaldehyde for 48 h. Micro-computed tomography (micro-CT) was then conducted to assess bone alterations. Finally, decalcified sections of the femurs were prepared and subjected to histological staining for further analysis.

Statistical analyses

The data are shown as the means ± standard deviations (SDs) and were analyzed via GraphPad Prism 9 (GraphPad Software, USA). Comparisons among treatment groups were conducted via analysis of variance (ANOVA). A significance level of $p < 0.05$ was considered statistically significant. The average fluorescence intensities were determined via ImageJ software.

Reporting summary

Further information on research design is available in the Nature Portfolio Reporting Summary linked to this article.

Data availability

The lipidomics data generated in this study have been deposited in the Open Archive for Miscellaneous Data (OMIX) database of the National Genomics Data Center (NGDC) under accession code OMIX011181. All data supporting the article are included in the main article, Supplementary Information and the Source Data file. Source data are provided with this article. Source data are provided with this paper.

References

1. Wang, Y. et al. Bone marrow adipocyte: origin, biology and relationship with hematological malignancy. *Int. J. Lab. Hematol.* **46**, 10–19 (2024).

2. Hardouin, P., Rharass, T. & Lucas, S. Bone marrow adipose tissue: to be or not to be a typical adipose tissue? *Front. Endocrinol.* **7**, 85 (2016).

3. Cawthorn, W. P. et al. Bone marrow adipose tissue is an endocrine organ that contributes to increased circulating adiponectin during caloric restriction. *Cell Metab.* **20**, 368–375 (2014).

4. Scheller, E. L., Burr, A. A., MacDougald, O. A. & Cawthorn, W. P. Inside out: Bone marrow adipose tissue as a source of circulating adiponectin. *Adipocyte* **5**, 251–269 (2016).

5. Sulston, R. J. & Cawthorn, W. P. Bone marrow adipose tissue as an endocrine organ: close to the bone? *Horm. Mol. Biol. Clin. Investig.* **28**, 21–38 (2016).

6. Horowitz, M. C. et al. Bone marrow adipocytes. *Adipocyte* **6**, 193–204 (2017).

7. Liu, X. et al. Oxylipin-PPARγ-initiated adipocyte senescence propagates secondary senescence in the bone marrow. *Cell Metab.* **35**, 667–684.e666 (2023).

8. Xia, W. et al. Obesity causes mitochondrial fragmentation and dysfunction in white adipocytes due to RalA activation. *Nat. Metab.* **6**, 273–289 (2024).

9. Yamauchi, S. et al. Mitochondrial fatty acid oxidation drives senescence. *Sci. Adv.* **10**, eado5887 (2024).

10. Miwa, S., Kashyap, S., Chini, E. & von Zglinicki, T. Mitochondrial dysfunction in cell senescence and aging. *J. Clin. Investig.* **132**, e158447 (2022).

11. Escrig-Larena, J. I., Delgado-Pulido, S. & Mittelbrunn, M. Mitochondria during T cell aging. *Semin. Immunol.* **69**, 101808 (2023).

12. Li, Y. et al. Distinct metabolism of bone marrow adipocytes and their role in bone metastasis. *Front. Endocrinol.* **13**, 902033 (2022).

13. Li, J., Chen, X., Lu, L. & Yu, X. The relationship between bone marrow adipose tissue and bone metabolism in postmenopausal osteoporosis. *Cytokine Growth Factor Rev.* **52**, 88–98 (2020).

14. Beekman, K. M. et al. Osteoporosis and bone marrow adipose tissue. *Curr. Osteoporos. Rep.* **21**, 45–55 (2023).

15. Chang, S. F., Yeh, C. C., Chen, P. J. & Chang, H. I. The impact of lipid types and liposomal formulations on osteoblast adiposity and mineralization. *Molecules* **23**, 95 (2018).

16. Lee, J. et al. Nucleic acid scavenging microfiber mesh inhibits trauma-induced inflammation and thrombosis. *Biomaterials* **120**, 94–102 (2017).

17. Pisetsky, D. S., Lee, J., Leong, K. W. & Sullenger, B. A. Nucleic acid-binding polymers as anti-inflammatory agents: reducing the danger of nuclear attack. *Expert Rev. Clin. Immunol.* **8**, 1–3 (2012).

18. Mariman, E. C. & Wang, P. Adipocyte extracellular matrix composition, dynamics and role in obesity. *Cell. Mol. Life Sci.* **67**, 1277–1292 (2010).

19. Puri, S., Coulson-Thomas, Y. M., Gesteira, T. F. & Coulson-Thomas, V. J. Distribution and function of glycosaminoglycans and proteoglycans in the development, homeostasis and pathology of the ocular surface. *Front. Cell Dev. Biol.* **8**, 731 (2020).

20. Li, J., Liang, H., Liu, J. & Wang, Z. Poly (amidoamine) (PAMAM) dendrimer mediated delivery of drug and pDNA/siRNA for cancer therapy. *Int. J. Pharm.* **546**, 215–225 (2018).

21. Wan, Q. et al. Selective targeting of visceral adiposity by polycation nanomedicine. *Nat. Nanotechnol.* **17**, 1311–1321 (2022).

22. Lee, J. Y., Kim, W. K., Bae, K. H., Lee, S. C. & Lee E. W. Lipid metabolism and ferroptosis. *Biology* **10**, 184 (2021).

23. Yalcinkaya, T., Uzilday, B., Ozgur, R., Turkan, I. & Mano, J. Lipid peroxidation-derived reactive carbonyl species (RCS): their interaction with ROS and cellular redox during environmental stresses. *Environ. Exp. Bot.* **165**, 139–149 (2019).

24. Wu, T. et al. Bimetal biomimetic engineering utilizing metal–organic frameworks for superoxide dismutase mimic. *ACS Mater. Lett.* **4**, 751–757 (2022).

25. Rosa, A. C. et al. Strategies to expand the therapeutic potential of superoxide dismutase by exploiting delivery approaches. *Int. J. Biol. Macromol.* **168**, 846–865 (2021).

26. Huang, T. et al. Targeting adipocyte ESRRA promotes osteogenesis and vascular formation in adipocyte-rich bone marrow. *Nat. Commun.* **15**, 3769 (2024).

27. Li, H. et al. 11β-Hydroxysteroid dehydrogenase type 1 facilitates osteoporosis by turning on osteoclastogenesis through Hippo signaling. *Int. J. Biol. Sci.* **19**, 3628–3639 (2023).

28. Guerra, I. M. S. et al. Mitochondrial fatty acid β-oxidation disorders: from disease to lipidomic studies-a critical review. *Int. J. Mol. Sci.* **23**, 13933 (2022).

29. Ribas, G. S. & Vargas, C. R. Evidence that oxidative disbalance and mitochondrial dysfunction are involved in the pathophysiology of fatty acid oxidation disorders. *Cell. Mol. Neurobiol.* **42**, 521–532 (2022).

30. Lin, X. et al. Smart nanosacrificial layer on the bone surface prevents osteoporosis through acid-base neutralization regulated biocascade effects. *J. Am. Chem. Soc.* **142**, 17543–17556 (2020).

31. Liu, X. et al. Metal-polyDNA nanoparticles reconstruct osteoporotic microenvironment for enhanced osteoporosis treatment. *Sci. Adv.* **9**, eadf3329 (2023).

32. Xia, X. et al. Role of oxidative stress in the concurrent development of osteoporosis and tendinopathy: emerging challenges and prospects for treatment modalities. *J. Cell. Mol. Med.* **28**, e18508 (2024).

33. Yuan, H. et al. Natural metal polyphenol nanozyme: free radical scavenging and antioxidation for the treatment of acute kidney injury. *ACS Mater. Lett.* **5**, 2807–2819 (2023).

34. Gu, Y., Han, J., Jiang, C. & Zhang, Y. Biomarkers, oxidative stress and autophagy in skin aging. *Ageing Res. Rev.* **59**, 101036 (2020).

35. Fang, S., Wu, S. & Chen, P. Targeting Caveolin-1 for enhanced rotator cuff repair: findings from single-cell RNA sequencing. *Cell Death Discov.* **11**, 88 (2025).

36. Zong, Y. et al. Mitochondrial dysfunction: mechanisms and advances in therapy. *Signal Transduct. Target. Ther.* **9**, 124 (2024).

37. Jana, B. A., Chintamaneni, P. K., Krishnamurthy, P. T., Wadhwani, A. & Mohankumar, S. K. Cytosolic lipid excess-induced mitochondrial dysfunction is the cause or effect of high fat diet-induced skeletal muscle insulin resistance: a molecular insight. *Mol. Biol. Rep.* **46**, 957–963 (2019).

38. Da, W., Jiang, W. & Tao, L. ROS/MMP-9 mediated CS degradation in BMSC inhibits citric acid metabolism participating in the dual regulation of bone remodelling. *Cell Death Discov.* **10**, 77 (2024).

39. Rong, X. et al. Lpcat3-dependent production of arachidonoyl phospholipids is a key determinant of triglyceride secretion. *eLife* **4**, e06557 (2015).

40. Yu, W. et al. Bone marrow adipogenic lineage precursors promote osteoclastogenesis in bone remodeling and pathologic bone loss. *J. Clin. Investig.* **131**, e140214 (2021).

41. Huang, B. et al. Polycationic PAMAM ameliorates obesity-associated chronic inflammation and focal adiposity. *Biomaterials* **293**, 121850 (2023).

42. Wang, Y. J. et al. Cholesterol and fatty acids regulate cysteine ubiquitylation of ACAT2 through competitive oxidation. *Nat. Cell Biol.* **19**, 808–819 (2017).

43. Liu, C. et al. CHD7 regulates bone-fat balance by suppressing PPAR-γ signaling. *Nat. Commun.* **13**, 1989 (2022).

44. Nelson, T. A., Tommasini, S. & Fretz, J. A. Deletion of the transcription factor EBF1 in perivascular stroma disrupts skeletal homeostasis and precipitates premature aging of the marrow microenvironment. *Bone* **187**, 117198 (2024).

45. Chen, H. et al. Prostaglandin E2 mediates sensory nerve regulation of bone homeostasis. *Nat. Commun.* **10**, 181 (2019).

Author contributions

H.C., S.H., H.W., and W.L. conceived the study and design of the study. W.L. performed most of the experiments. S.G., H.W., and S.H. contributed to the lipidomic analysis and the synthesis and characterization of CZP@LC. S.H., X.Z., D.Z., and K.L. participated in the animal modeling, analyzed and interpreted the data. B.M., C.P., Z.X., and T.L. contributed to the preprocessing and quality assessment of the data. W.L., D.Z., S.H., and S.G. wrote the manuscript. H.C. and H.W. made constructive suggestions and revised the manuscript. All authors contributed to the critical review of the manuscript.

Competing interests

The authors declare no competing interests.

Additional information

Supplementary information The online version contains supplementary material available at https://doi.org/10.1038/s41467-025-63376-4.

Correspondence and requests for materials should be addressed to Huihui Wang, Sihan Hu or Hao Chen.

Peer review information *Nature Communications* thanks the anonymous reviewers for their contribution to the peer review of this work. A peer review file is available.

Reprints and permissions information is available at http://www.nature.com/reprints

Publisher's note Springer Nature remains neutral with regard to jurisdictional claims in published maps and institutional affiliations.